METHODS FOR QUANTITATIVE ANALYSIS OF IN-VIVO BONE MICROSTRUCTURE USING COMPUTED TOMOGRAPHY

by

Shalini Subramanian

A thesis submitted to Johns Hopkins University in conformity with the requirements for the degree of Master of Science and Engineering

Baltimore, Maryland

May 2019

ABSTRACT

Bone health can be assessed by observing alterations in trabecular microarchitecture. These alterations are an early indicator for a range of musculoskeletal diseases ranging from osteoporosis to osteoarthritis. Fractures due to loss of bone are also seen in patients undergoing radiation therapy. Early detection of changes in the trabecular microstructure can be used to help design protocols and therapies targeting the factors affecting bone health. *In-vivo* evaluation if bone microarchitecture is still a challenge due to the limited spatial resolution provided by conventional computed tomography (CT). In this thesis, we investigate different high-resolution modalities to perform quantitative analysis of trabecular bone. New diagnostic imaging modalities with enhanced spatial resolution include Cone Beam CT (CBCT) systems with flat-panel detectors (FPD) and CMOS detectors. The FPD and CMOS detectors offer higher spatial resolution than the detectors in Conventional CT. Another example of a new modality with potential application in the imaging of trabecular microstructures is a recently introduces ultra–high resolution (UHR) multi-detector CT which has ~2x better spatial resolution than Conventional CT (Aquilion Precision CT, Canon Medical). We also investigate the performance of this novel Precision CT for trabecular microstructure imaging. The modalities are evaluated using bone morphometry parameters extracted from the

scanned volumes. Bone metrics (including BV/TV, Tb.Th, Tb.Sp, and Tb.N, each defined below) are computed from the images obtained from CMOS-CBCT, FPD-CBCT, Conventional CT and Precision CT. These values are compared with the bone metrics obtained from analysis performed on Micro-CT (which is taken as a 'gold standard' reference and basis of comparison). Those studies involved imaging of cadaveric bone samples. A patient study is also performed to assess the feasibility of imaging trabecular structures in realistic clinical scenarios as opposed to a controlled experimental environment while imaging cadaveric samples. In cadaveric samples, imaging using CBCT achieves improved performance in quantification of bone microstructure. The methods and results offer motivation and a platform for ongoing development of quantitative imaging and evaluation of bone health in osteoporosis, osteoarthritis and bone loss due to radiation therapy.

THESIS COMMITTEE

Dr. Wojciech Zbijewski

Assistant Professor

Department of Biomedical Engineering

The I-STAR Laboratory (http://istar.jhu.edu/)

Johns Hopkins University

Dr. Jeffrey H. Siewerdsen

John C. Malone Professor and Vice-Chair, Department of Biomedical Engineering

Co-Director, The Carnegie Center for Surgical Innovation (http://carnegie.jhu.edu)

The I-STAR Lab (http://istar.jhu.edu)

Johns Hopkins University

Dr. Carol Morris

Associate Professor, Department of Orthopaedic Surgery

Division Chief, Orthopaedic Oncology

Johns Hopkins Medicine

ACKNOWLEDGEMENT

The following people had a significant influence on this thesis: Dr. Wojciech Zbijewski, Dr. Michael Brehler, and Cao Qian (Department of Biomedical Engineering, Johns Hopkins University).

I'd also like to thank all the members of the I-STAR Lab.

TABLE OF CONTENTS

LIST OF TABLES ……..viii

LIST OF FIGURES ix

CHAPTER 1 1

Introduction 1

1.1 Significance 1

1.2 Quantitative Assessment of Bone Microarchitecture 4

1.3 The Role of Imaging in Assessment of Bone Quality 5

1.4 Thesis Overview and Outline 6

CHAPTER 2 8

Methods 8

2.1 Imaging Systems and Imaging Protocols 8

2.2 Validation in Bone Samples 11

2.3 Clinical Translation: Radiation Therapy Study 19

CHAPTER 3 24

Results and Discussion 24

3.1 Validation Studies 24

3.2 Evaluation of UHR-MDCT 31

3.3 RT Patient Data Processing 32

CHAPTER 4 37

Conclusion 37

References 39

APPENDIX 42

Biography 48

LIST OF TABLES

Table 1: Comparison between FPD-CBCT and CMOS-CBCT systems 9

Table 2: Comparison between NR-MDCT protocol and UHR-MDCT protocol..... 15

Table 3: Acquisition and Reconstruction parameters for the RT patient study 20

LIST OF FIGURES

Figure 1: Metrics of bone microarchitecture. 5

Figure 2: Extremity CBCT scanner in weight bearing and unloaded configuration 8

Figure 3: Detector MTF Measurements 10

Figure 4: Axial Slice of Cadaveric Tibia 12

Figure 5: Experimental Setup 13

Figure 6: Axial Slice of Cadaveric ulna imaged using (A) Micro-CT, (B) UHR-MDCT and (C) NR CT 15

Figure 7: Segmentation framework 16

Figure 9: Steps involved preparing data to get reconstructions. 21

Figure 10: Two step registration process 22

Figure 11: Grayscale axial slices of Cadaveric tibia samples 24

Figure 12: Pearson Correlation coeficient maps for CMOS-CBCT, FPD-CBCT and Conventional CT along with segmentations resulting in highest correlations 26

Figure 13: Axial Slices of optimal segmentations for Micro-CT, CMOS-CBCT, FPD-CBCT and Conventional CT 27

Figure 14: Comparison of metrics of trabecular microarchitecture 28

Figure 15: Axial slices of grayscale and segmentations of 3 samples of Micro-CT, and CBCT 29

Figure 16: Comparison of metrics of trabecular microarchitecture for CBCT (effect of resolution study) 30

Figure 17: Axial and Sagital view of ROI in UHR-CT and NR-CT. 31

Figure 18: Axial slices of image reconstruction of visit 1 for patient 4 and 6 (1st column), visit 5 (2nd column) and difference image (3rd column) 32

Figure 19:Axial slice of water phantom before and after scatter correction 33

Figure 20: Distribution of grayscale values of calibration inserts before and after scatter correction 34

Figure 21: Axial slice of a knee scan before and after scatter correction 35

CHAPTER 1

Introduction

1.1 Significance

Deterioration in bone health is a significant concern amongst the US population. A broad range of Musculoskeletal (MSK) disease affecting bone health includes Osteoarthritis (OA) and Osteoporosis (OP). Bone health of individuals is associated with alteration in trabecular microarchitecture which offers an early indicator in detecting OA and OP. Understanding changes in trabecular microarchitecture can also help detect radiation-induced bone loss that leads to increased risk of fractures in patients undergoing Radiation Therapy (RT). Overall, trabecular microarchitecture is an important determinant of bone health. However, performing quantitative analysis of alterations in bone microarchitecture is challenging due to the limited spatial resolution provided by conventional multi-detector CT (MDCT). The performance of new imaging modalities like extremity CBCT and recently introduced Ultra-High Resolution MDCT (UHR-MDCT – for example, the Aquilion Precision scanner, Canon Medical) are evaluated for this purpose.

1.1.1 Osteoarthritis

Osteoarthritis (OA) is the most common degenerative joint disease and a leading cause of disability, afflicting ~30 million US adults and growing in prevalence due to increased frequency of obesity and aging of the population [1]. It is a multi-factorial disease exacerbated by the lack of effective treatment, with arthroplasty often the only therapeutic solution. The occurrence of OA is closely related to the shape and location of the joint [3]. The risk of OA in the hips and knees is considerably high, and early detection of OA can help facilitate therapies that eliminate the need for arthroplasty. Clinical evidence suggests that initiation of OA is associated with decreased bone density and stiffening of subchondral bone (SB) [9]. Stiffening is associated with thickening of the subchondral cortical plate, increase in number of trabeculae, SB sclerosis, and formation of osteophytes [3]. In later stages of OA the microarchitecture of SB is weakened, resulting in abnormal alterations in the pattern of the trabeculae.

1.1.2 Osteoporosis

OP is a metabolic disorder, resulting in reduced bone mass and deterioration of bone structures [10]. The bone weakens to a point that it can break easily. It is most common in an aging population and it often goes undetected until a bone breaks. Approximately 16% of U.S adults aged 65 years and over have been detected with OP and low bone mass at the femoral neck or lumbar spine regions [12]. Age related OP was higher among women (~24%) than in men (5.6%) [11]. Hormonal changes occurring in individuals over a period of time lead to bone resorption. Weakening of

the bone structure combined with the cumulative result of minimal trauma experienced by the bone from day to day activities causes OP [13]. It is most common in the bones in hip, backbone (vertebrae) and wrist. On examination of sites affected by OP, it was seen that the density and microarchitecture is no longer uniform throughout the trabecular compartment. The microarchitecture of the trabeculae is altered from normal microstructural alignment. Diagnosis of OP is frequently based on measurements of Bone Mineral Density (BMD). BMD is compared to an established norm of a healthy young adult and reported in terms of standard deviations. A score of 0 indicates healthy individuals. A score between -1 to +1 is considered normal or health. Values below -1 indicate that the individual is prone to fractures. A score below 2.5 is considered as osteoporosis. A negative value indicates you have low bone mass [22].

1.1.3 Bone Loss in Radiotherapy

Deterioration of bone health is also seen in patients undergoing Radiation Therapy (RT). Fractures due to bone loss are a relatively common occurrence in RT patients. There is a strong variability in RT-induced fractures (e.g. 1.8% – 19% in ribs following breast RT [20], 1.2% -25% in lower extremity following irradiation of sarcomas [21]. Imaging of bone microarchitecture can help detect and quantify radiation induced bone loss. These imaging biomarkers are necessary to help design RT protocols minimizing bone loss. Measuring bone morphometry parameters and volumetric BMD (vBMD) can help study the possible effects of RT.

1.2 Quantitative Assessment of Bone Microarchitecture

Early detection of OP and OA involves measurement of bone morphometry features from the trabecular structures. In OA, alterations in SB leads to reduction in Bone Volume to Tissue Volume ratio (BV/TV), decrease in Trabecular Thickness (Tb.Th) and increased Trabecular Spacing (Tb.Sp). Fig. 1 shows a simplified representation of those measurements. Tb.Th is obtained from the mean width of the trabeculae within a Region of Interest (ROI). Tb.Sp is the mean size of "cavities" of bone marrow present within the ROI. Another important bone metric used to assess bone health is Trabecular Number (Tb.N), defined as the inverse of the distance between the mid-axes of the trabeculae. In OP, TbSp and degree of anisotropy (AI) is high at affected locations [14].

The conventional methods of trabecular micro-morphometry include a segmentation step to delineate the trabecular ridges from the background. To achieve accurate segmentations representing the trabecular ridges in Micro-CT systems, global thresholding is often sufficient. In systems with limited spatial resolution, achieving robust segmentation typically requires using a spatially varying threshold based on local image properties [15, 16]. Bone morphometry features are computed from the segmentations using a sphere fitting algorithm (Fig. 1) [11].

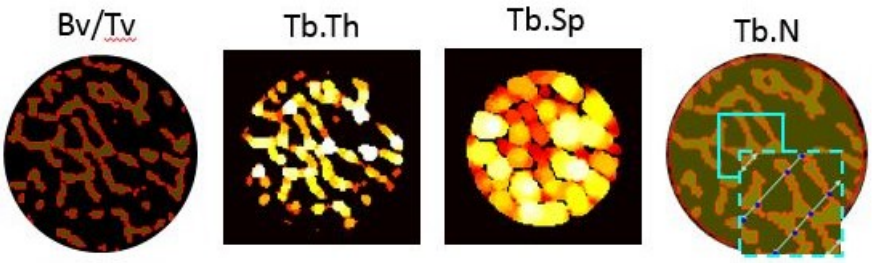

Figure 1: Metrics of bone microarchitecture.

1.3 The Role of Imaging in Assessment of Bone Quality

Progression of OA and OP in affected individuals is currently assessed clinically using radiography. Using in vivo Micro-CT has been established as the gold standard to analyze the architecture of SB at trabecular level. In recent times, there has been more emphasis on radiography using magnification techniques to assess bone quality. Increased use of quantitative CT (QCT) has been used in monitoring bone health. QCT focuses on bone mineral density (BMD) to predict osteoporosis or osteoarthritis. Using QCT to compute the micro-architectural parameters is challenged by its limited spatial resolution. Conventional MDCT has a spatial resolution of about 250-300 μm, compared to ~50-200 μm size of trabeculae.

Cone Beam CT (CBCT) scanners help overcome this limitation with Flat Panel Detectors (FPD) having a relatively high spatial resolution – for example, pixel size ~150 μm, compared to ~500 μm for MDCT. The FPD-CBCT system used in the work described below is a dedicated scanner for imaging of extremities. The advantages of using an extremity FPD-CBCT over a MDCT system has higher spatial resolution, and novel capability for volumetric weight bearing imaging [7]. Trabecular bone metrics

obtained with extremity CBCT have also achieved high correlation (~0.9) with gold standard Micro-CT [2]. To further enhance the performance of extremity CBCT imaging of bone micro-architecture, a new system was developed by replacing the FPD with a custom CMOS detector. The CMOS technology offers higher frame rate, smaller detector pixels (~99 μm) and lower electronic noise than the FPD-CBCT scanner [8].

Apart from extremity CBCT, an UHR-MDCT has recently been introduced (Canon Precision UHR CT). The system enables >2x improved spatial resolution (~150 μm detail size) compared to current generation MDCT. Among clinical applications that might benefit from the enhanced spatial resolution is assessment of microstructural factors affecting bone strength in spine and hips.

1.4 Thesis Overview and Outline

Thesis Statement: New imaging systems with improved spatial resolution in comparison to conventional MDCT could enable quantitative analysis of *in-vivo* bone micro-architecture, providing the ability to monitor bone health and facilitate early detection of OA and OP.

Chapter 2 discusses the current development and challenges in performing *in-vivo* evaluations of alterations that occur in bone microstructure due to OA, OP, RT or other musculoskeletal diseases. One of the main challenges is posed by the limited resolution that conventional orthopedic imaging modalities provide. We evaluate the performance of newly developed extremity CBCT, and the recently introduced UHR-MDCT system with high spatial resolution against gold standard Micro-CT in imaging trabecular microstructure. Performance

of each of these systems was evaluated by computing the bone metrics using segmentations generated from image volumes of bone samples. The segmentation pipeline used on the bone samples is discussed in detail in Chapter 2. Initial experiments study the efficiency of the different systems available using bone core samples in a controlled environment. To translate the bone imaging capabilities to clinical applications, we analyze data from a study with 20 patients undergoing RT scanned using a dedicated extremity FPD-CBCT system. The study involved imaging of these patients over a period of time to determine bone loss occurring following RT. The pre-processing of the data obtained from the scanner to enable longitudinal assessment of bone quality is discussed in detail.

Chapter 3 presents the results and analysis obtained from the sample datasets. The quantitative analysis included computing the Pearson correlation coefficient of bone metric values obtained with gold standard Micro-CT. Extremity CBCT achieved high correlation with Micro-CT in comparison to conventional MDCT. Similarly, results obtained on evaluating the performance of the UHR-MDCT system were reported in terms of correlation with Micro-CT. Chapter 3 also presents the performance of the processing pipeline developed for RT patient data obtained from extremity scanners.

CHAPTER 2

Methods

2.1 Imaging Systems and Imaging Protocols

High resolution images were acquired using the extremity CBCT (FPD- and CMOS-based) and UHR-MDCT.

The FPD-CBCT and CMOS-CBCT systems were based on the Onsight3D extremity scanner (Carestream Health, Rochester NY). The scanner is designed to support weight bearing imaging in a natural standing stance (Figure 2).

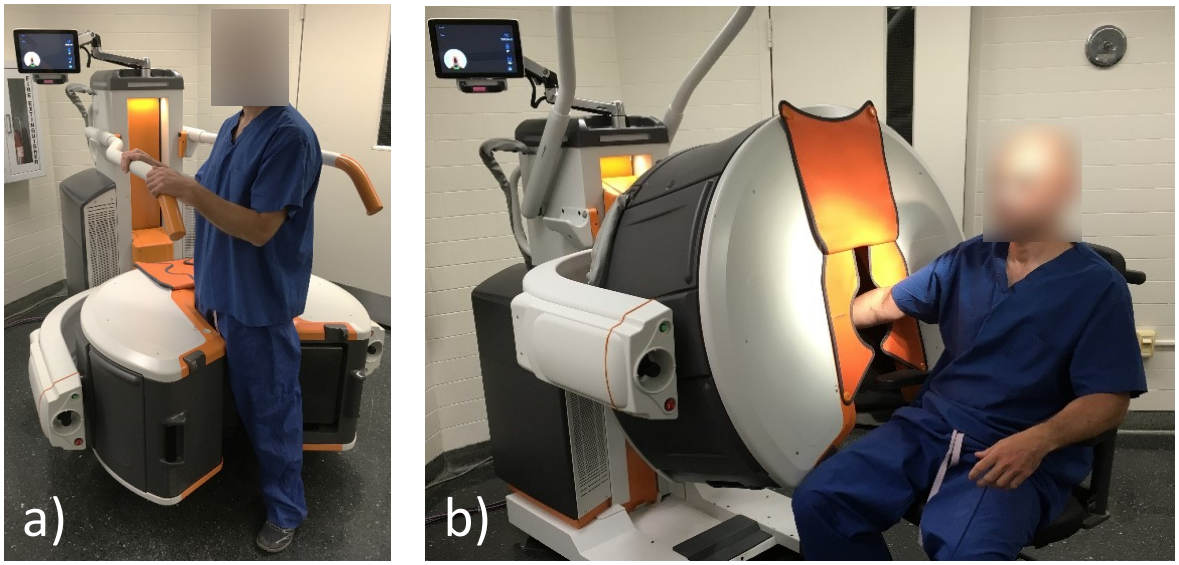

Figure 2: (A) Extremity CBCT in configuration for weight-bearing imaging (B) Extremity CBCT in unloaded configuration for imaging lower or upper extremity

The gantry design accommodates motion of the detector and source around the patients' legs during the scan. The same system can be used to image unloaded upper or lower extremities by changing the height and angulation of the gantry as shown in Figure 2. Experiments were performed using a FPD-CBCT and CMOS-CBCT in the weight bearing configuration of the knee, keeping the samples positioned in the center of the field of view. The samples were also scanned using a conventional MDCT system, for comparison.

The main difference between the two CBCT systems can be seen in Table 1.

	a-Si:H FPD-CBCT	**CMOS-CBCT**
Detector	Varex PaxScan2530 a-Si FPD	Dalsa Xineos3030 CMOS
Pixel size	139 μm	99 μm
Scintillator thickness	~0.7 mm	~0.4 mm
e^- noise	~2000 e^-	~140 e^-
Frame Rate	Up to 7.5 fps (full res.)	Up to 30 fps (full res.)
X-ray source	Three source Stationary anode*	Single source, Rotating anode
Focal spot	0.5	0.3

Table 1: Comparison between FPD-CBCT and CMOS-CBCT systems

The CMOS detector has a detector pixel size of 99 μm, compared to 137 μm for the a-Si:H FPD. The smaller pixel detector size combined with a reduced scintillator thickness in the CMOS detector improves the spatial resolution in images obtained using the CMOS-CBCT system. The improved spatial resolution of the CMOS-CBCT over FPD-CBCT can be seen in Figure 3. The MTF plot shows that CMOS-CBCT has better performance, with two-fold improvement at the Nyquist frequency. (5 mm^{-1}) [7].

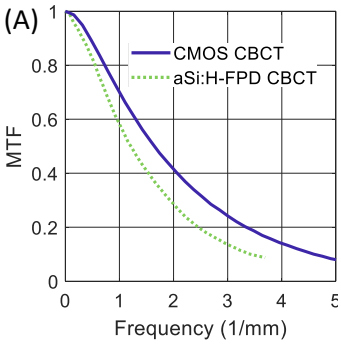

Figure 3: Detector MTF measurements

The data obtained from FPD-CBCT and CMOS-CBCT were reconstructed using the Feldkamp 3D filtered-back projection algorithm using a Hann apodization filter with cutoff at 0.7 times the Nyquist frequency. Voxel size was 75 μm. All CBCT reconstructions were converted to BMD units using a calibration phantom. The reference Micro-CT image volumes were obtained on a Micro-CT 35 unit (Scanco Medical, Pennsylvania). The Micro-CT voxels measured 15 μm.

The UHR-MDCT system is a novel high-resolution MDCT scanner with ~150 μm pixel size (2x improved spatial resolution) and smaller focal spot size (0.4 mm x 0.5 mm) than conventional MDCT. The samples were imaged using two protocols on this system, summarized in Table 2 (Sec. 2.2.1.2). The Ultra High Resolution (UHR) acquisition, with 0.25 mm slice thickness, 1796 detector channels, 160 detector rows and x-ray tube focal spot size of 0.4 mm x 0.5 mm was used. The other protocol was a Normal

Resolution (NR) protocol reflecting the current generation of MDCT. The NR protocol implemented 0.5 mm slice thickness, 896 channels, 80 rows, and a focal spot size of 0.8 mm x 1.3 mm. Scans from both protocols were reconstructed using sharp kernels (FC30 as named by the manufacturer).

2.2 Validation in Bone Samples

A study performed to evaluate the performance of the FPD-CBCT and CMOS-CBCT involved computing the bone metrics for bone core samples extracted from cadaveric tibia, and comparing them against gold standard Micro-CT. Along with extremity CBCT scanner, the bone cores were also imaged using conventional MDCT. Another study including imaging the cadaveric ulna was performed to evaluate the ability of the UHR-MDCT system in imaging trabecular microstructure.

2.2.1 Sources of Data

2.2.1.1 Extremity CBCT

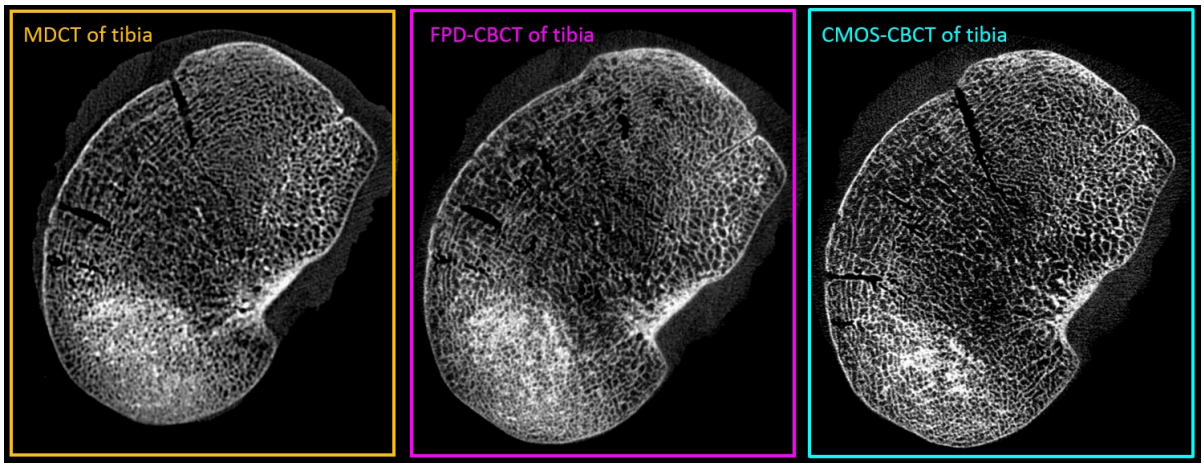

Figure 4: Axial Slice of Cadaveric tibia scanned using MDCT, FPD-CBCT and CMOS-CBCT

The extremity data used in evaluating the extremity CBCT consists of 26 cores extracted from 4 human cadaveric tibias obtained in collaboration with the Hospital for Special Surgery (HSS, New York NY). Intact tibias were initially scanned using MDCT, FPD-CBCT and CMOS-CBCT. Figure 4 shows example axial slice reconstructions from each system. CBCT qualitatively exhibits better detail in trabecular microstructures in comparison to MDCT.

Twenty-Six cores, each ~8 mm in diameter, were extracted from the four cadaveric tibias. A custom drilling and cutting guide was 3D printed for each tibia to enable

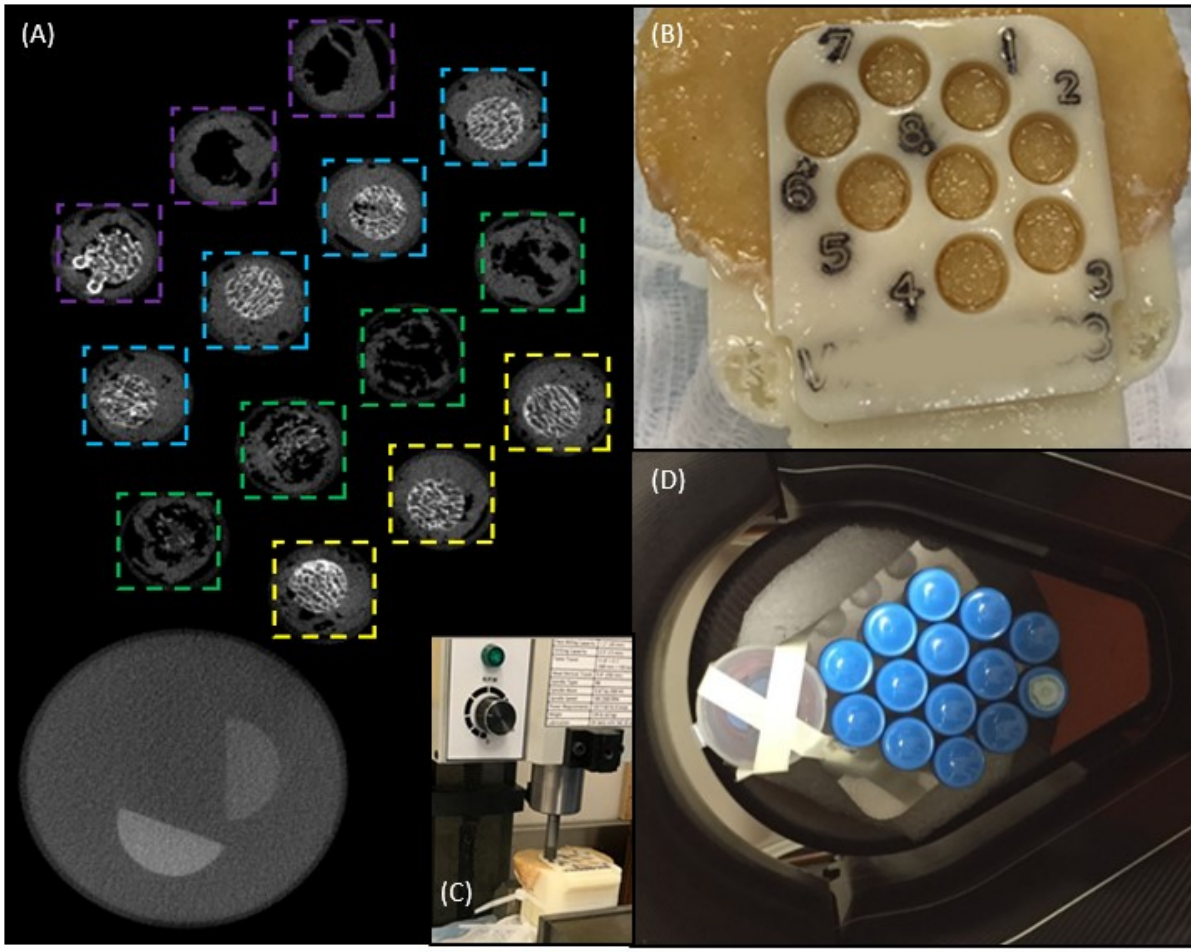

Figure 5: (A) Axial Slice of the configuration of 26 samples obtained from 4 cadaveric tibia placed along with BMD inserts. (B) Custom 3D printed cutting guide. (C) Cutting and drilling setup. (D) Top view of samples placed inside an extremity CBCT

precise removal of proximal articular surfaces and accurate positioning of bone cores. The custom guide was built using the initial MDCT scans. Using the guide, the tibial plateau was removed using an oscillating saw and 5-8 coring kerfs were drilled in the exposed trabecular bone of each specimen. Before cutting the tibia distally, post coring MDCT scans were obtained, which (combined with bone specific drill guides) enabled accurate localization of the cores.

The tibias were cut distally perpendicular the tibial shaft at ~32 mm from the exposed trabecular region. All cores were imaged using MDCT, FPD-CBCT and CMOS-CBCT. In the same field of view, a water cylinder of ~50 mm diameter was placed along with BMD calibration inserts of each 75 mg/mL CaHA and 150 mg/mL CaHA and the samples. The configuration of the samples placed in the field of view is illustrated in Figure 5.

The cores were individually imaged on a Micro-CT system. The ability of the CBCT systems to delineate trabecular microarchitecture is reported in comparison to the metrics of trabecular microarchitecture obtained from gold standard Micro-CT.

We also performed a study with 35 transiliac bone biopsy samples to study the effects of spatial resolution on the ability to predict the bone metrics. These samples were imaged using the FPD-CBCT and the results were compared against the values obtained for the Micro-CT.

2.2.1.2 Ultra-High-Resolution MDCT

A cadaveric ulna was imaged using the UHR-MDCT system using the UHR and NR protocols. NR-MDCT emulates conventional MDCT. Each bone sample was embedded in a plastic phantom of ~16 cm diameter for scanning purposes. The performance of the UHR-MDCT system was evaluated by computing bone metrics and comparing with Micro-CT. Figure 6 shows the axial slice of the ulna imaged using Micro-CT, UHR-MDCT and NR-MDCT. Micro-CT scans of the cadaveric ulna were

reconstructed at 28 μm voxel size. Table 2 shows the comparison between scan and reconstruction parameters for NR-MDCT and UHR-MDCT.

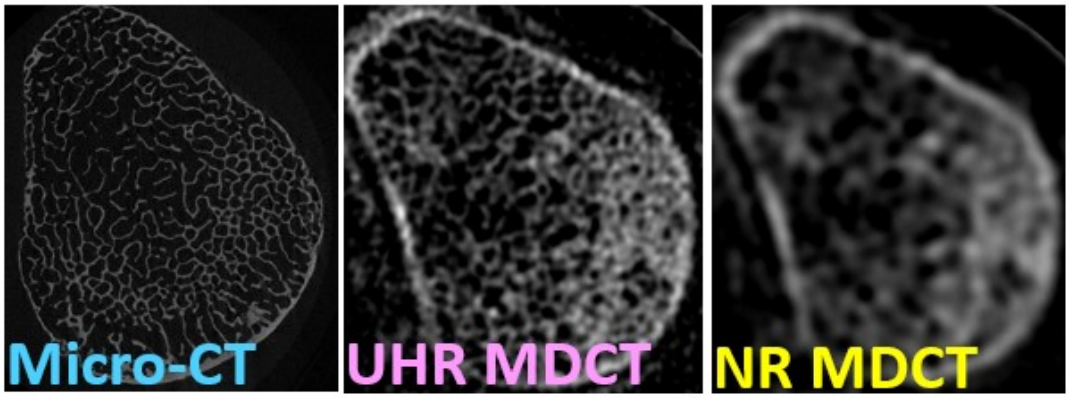

Figure 6: Axial Slice of Cadaveric ulna imaged using (A) Micro-CT, (B) UHR-MDCT and (C) NR MDCT

	NR-MDCT	**UHR-MDCT**
kVp	120 kVp	120 kVp
mAs	250 mAs	250 mAs
Nominal CTDI Dose	10.8 mGy	10.8 mGy
Scan Time	2.0 secs	2.7 secs
Focal Spot Size	0.8 mm x 1.3 mm	0.4 mm x 0.5 mm
Detector Channels	896 channels	1796 channels
Number of detector rows	80 rows	160 rows
Slice Thickness	0.5 mm	0.25 mm
Reconstruction Filter	FC30	FC30
Voxel Size (in-plane)	0.053 mm	0.0133 mm

Table 2: Comparison between NR-MDCT protocol and UHR-MDCT protocol

2.2.2 Image analysis pipeline for validation of CT-based measurements of bone microarchitecture

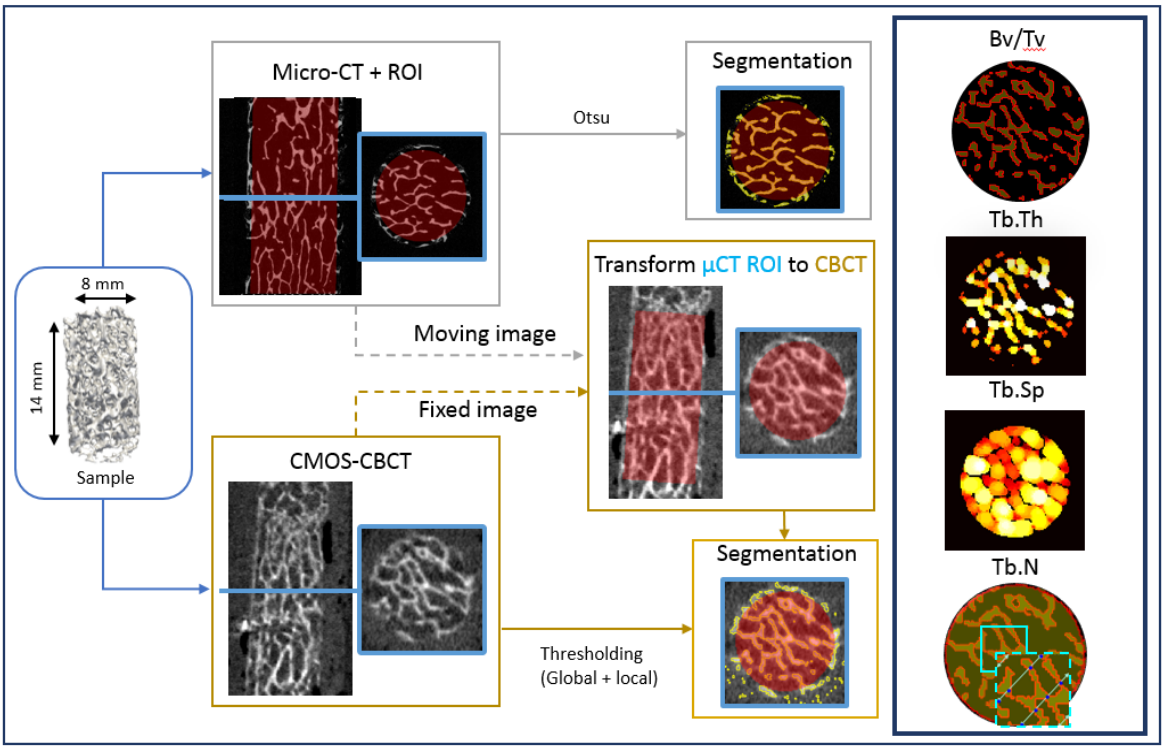

Figure 7: Framework to obtain binary segmentation of Micro-CT and CBCT volumes

We follow a previously developed framework to obtain trabecular measurements in CBCT and MDCT [2]. The pipeline used for processing Micro-CT and CBCT volumes is illustrated in Figure 7. The first step involves identifying the Region of Interest (ROI) in the Micro-CT scans of each core such that it avoids any cortical bone in the analysis. These binary ROI masks were then mapped to CBCT volumes/MDCT volumes using transforms obtained from rigid registration of Micro-CT and CBCT/MDCT reconstructions. Bone metrics were computed on the original

reconstructed dataset to avoid inaccurate measurements due loss of resolution. Only the masks were geometrically transformed to obtain the same ROI in each modality.

Binary bone segmentation of Micro-CT was obtained by applying Otsu's method to this original reconstructed data [5]. Otsu's thresholding method involves reduction of a grayscale image to a binary image by iterating through all possible threshold values. The optimal threshold is then obtained as the one that separates the two classes such that their combined spread (intra–class variance) is minimal [5].

2.2.2.1 Segmentation of CBCT and MDCT image volumes

For CMOS-CBCT, FPD-CBCT and MDCT a two-step approach involving a global pre-thresholding followed by Bernsen's thresholding was used. Bernsen's algorithm used for obtaining high-frequency trabecular features from extremity CBCT data made use of a user-provided contrast threshold and window size to perform segmentation. The local contrast inside a moving window was compared to the contrast threshold provided. If the local contrast (maximum intensity – minimum intensity within window region) was found to be less than the contrast threshold, the window was considered to be homogeneous and all the pixel was assigned the mid-grey value (the mean of the minimum and maximum grey values in the local window). If the local contrast was more than the contrast threshold, the window is separated into two classes based on whether the voxel value is less than or greater than the mid-grey value. An additional global pre-thresholding step was added before applying Bernsen to improve the accuracy of segmentations. In this step, a Gaussian was fit to the histogram of the

entire image volume and voxels below the FWHM were removed. This step removes a majority of background voxels from the image so that the local histogram consists mainly of bone voxels and soft-tissue voxels with elevated attenuation due to partial volume effect. It was seen that pre-thresholding helped in better delineation of trabecular structure [2].

The radius of the sliding window and the local contrast threshold within the sliding window are the two user defined parameters in the Bernsen algorithm which were adjusted to optimize the segmentation. A sweep across a range of these parameters was performed to determine optimal combination of window radius and local contrast threshold for each modality. The optimal combination was selected based on the Pearson correlation coefficient and a visual inspection of the segmentations. Bone morphometry features, fraction of Bone Volume to Tissue Volume (BV/TV), Trabecular Thickness (Tb.Th), Trabecular Spacing (Tb.Sp) and Trabecular Number (Tb.N) were computed from these binary segmentations. As discussed earlier, correlation coefficients were computed with gold standard Micro-CT to evaluate the performance of the segmentation algorithm and the CT system.

2.2.2.2 Segmentation of UHR-MDCT and NR-MDCT (Precision CT)

Binary bone segmentations of the MDCT volumes were obtained using Bernsen's local thresholding method. A parameter sweep was performed in this case as well to obtain optimal combination of Bernsen algorithm parameters. Micro-CT segmentations were obtained using Otsu's method. Bone metrics (BV/TV, Tb.Th and Tb.Sp) were

measured within 10 ROIs each (~3.5 x 3.5 x 3.5 mm^3) distributed at corresponding locations within CT and Micro-CT volumes. Correlations between the UHR-MDCT/NR-MDCT and Micro-CT were computed.

2.3 Clinical Translation: Radiation Therapy Study

The validation studies described above involved trabecular microarchitecture of bone samples extracted in a controlled environment. In the following study, RT patients were scanned to evaluate the feasibility and performance of extremity FPD-CBCT in imaging of trabecular microstructures in real world situations.

2.3.1 Clinical Pilot Study Design

A pilot study including 20 patients was planned to study the possible effects of RT on bone microstructure. The main criteria for inclusion in the study (following informed consent and IRB approval) pertained to a patient population with extremity soft tissue sarcoma that required radiation treatment. For each patient, high resolution tomographic data of the affected limb and the contralateral limb was obtained. The FPD-CBCT acquired for the contralateral limb serves as control. The FPD-CBCT system was operated in a high-resolution mode with no pixel binning and scan time of 40 sec. Table 3 has detailed description of the acquisition and reconstruction parameters for the scans obtained using FPD-CBCT. The patient was sitting during the scan to minimize motion artifacts. Reduction of involuntary motion and reproducible patient

positioning are important factors for the analysis of morphological change in longitudinal studies.

	a-Si:H FPD-CBCT
Detector	Varex PaxScan2530 a-Si FPD
Pixel size	139 μm
Scintillator thickness	~0.7 mm
X-ray source	Three source Stationary anode*
Focal spot	0.5
mA	8.5 mA, 20 ms
kVp	90 kVp
Hann Apodization and filter cutoff	0.5, 0.9

Table 3: Acquisition and Reconstruction parameters for the RT patient study

For each patient, scans were acquired before their RT and during their treatment phase. As mentioned earlier, to perform comparative studies to determine the presence of bone loss due to RT over a period of time, it is necessary to measure at the same region of the extremity. Hence, it is necessary to register the reconstructions. Zeng and Shiraz-Bhurwani developed a structured pipeline to process the data obtained from the scanners, perform the reconstructions, and apply geometric transforms, scatter correction [17], and the motion correction algorithm [18] to them.

Motion artifacts can cause blurring as well as streaks in the image, which deteriorate the quality of the images. Low quality images will affect the accuracy of the measurements obtained from these scans. Scatter reduces the contrast of the image and also induces cupping non-uniformities. If uncorrected, scatter artifacts may interfere with accurate quantification of bone density and microarchitecture. Streaks associated with scatter are more prominent in thicker regions of the patient – for example, the knee. The quality of the images can be improved by applying motion correction and scatter correction algorithms during the process of reconstruction.

2.3.2 Data Preprocessing

The data from the FPD-CBCT system was analyzed as follows. The raw data obtained from the FPD-CBCT scanner was first converted into projection data (log-corrected line integrals) and geometric data. Each patient received multiple scans owing to their repetitive visits and scanning of the affected and non-affected extremity during each visit. The data were categorized according to individual visit: each visit has two sets of data, one for the affected limb and the other for the unaffected limb.

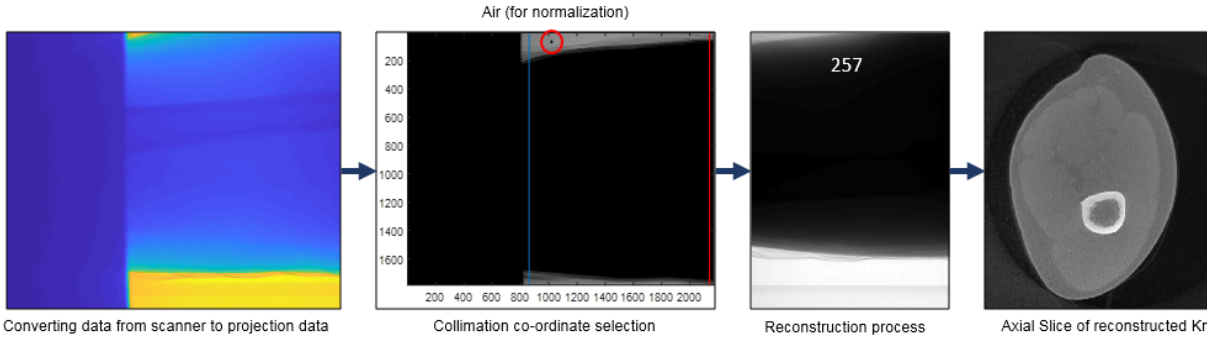

Figure 9: Steps involved in preparing scan data for 3D reconstruction.

The steps involved in preprocessing the scan data for 3D image reconstructions are shown in Figure 9.

These initial reconstructions were used to obtain geometric transforms for rigid registration between scans from the first visit and consequent visits. The registration process was a two-step approach explained in Figure 10. Preliminary manual registration was performed using MITK. The transform parameters were stored with respect to world origin coordinates. These transform parameters were applied to each scan during the process of image reconstruction. These image volumes reconstructed were further registered using Elastix. Figure 10 shows the process for ROI selection, where a small region is selected from these manually transformed reconstructions for finer registration using Elastix. Picking a smaller Region of Interest (ROI) for finer registration is crucial for regions like the ankle and hand, because of

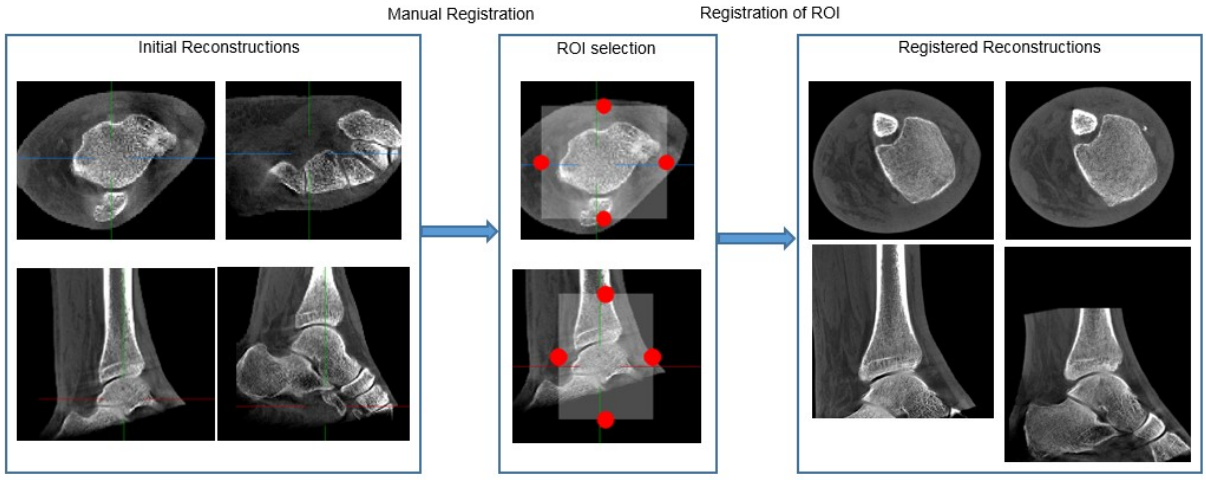

Figure 10: Two step registration process (Manual registration + ROI Elastix registration)

independent motion trajectories of each bone. The transform obtained after the final

registration of the smaller ROI is applied to the original projection data along with the initial geometric transform to get registered patient data. The final set of images in Figure 10 shows the image volumes that we obtain after applying transformations from MITK.

CHAPTER 3

Results and Discussion

3.1 Validation Studies

Figure 11 shows axial slices of 3 samples representing the range of trabecular thickness present in the sample study based on the cadaveric tibia. The gray scale images of Micro-CT, MDCT, FPD-CBCT and CMOS-CBCT were registered using rigid transformations for display purposes. The axial slices of Micro-CT show detailed trabecular microarchitecture. The CMOS-CBCT slices have lesser amount of blurring in comparison to the images obtained from FPD-CBCT and MDCT seen in the 2nd and 3rd column.

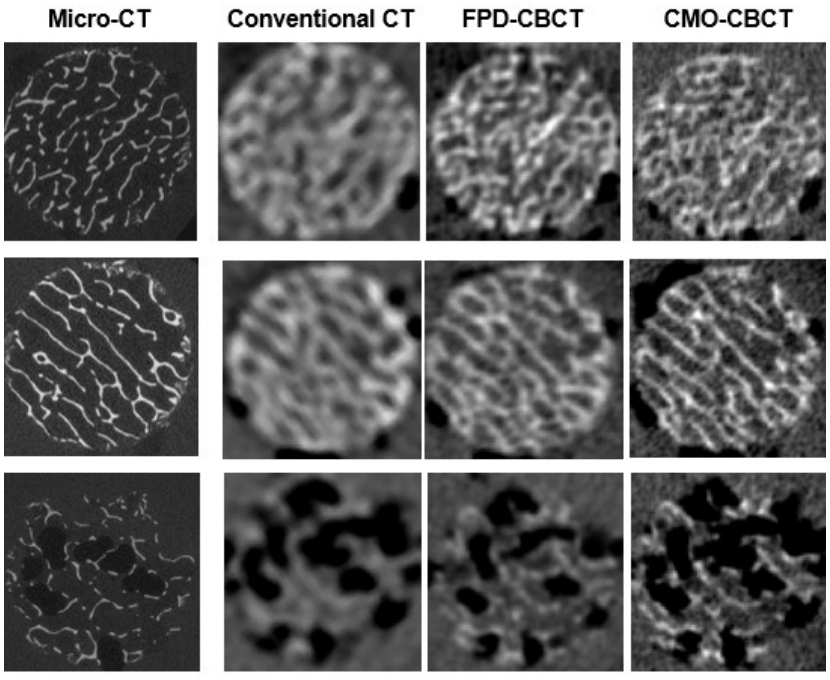

Figure 11: Axial Slices of Micro-CT (left column), Conventional MDCT (2nd Column), FPD-CBCT (3rd Column) and CMOS-CBCT (4th column) in grayscale.

Optimal segmentations for CBCT and MDCT were obtained by performing a Bernsen parameter sweep. The Bernsen's algorithm was applied to the volumes after global pre-thresholding. As discussed earlier Bernsen algorithm has two free parameters, the radius of the sliding window and the contrast threshold within the window. A sweep across a range of values was performed and segmentations for each combination of parameters was obtained. Pearson correlation coefficients were computed for bone metrics obtained for each of these with Micro-CT. Figure 12 shows correlation coefficient values across all possible combination of parameters for all three modalities. The highest correlation for each bone metric is highlighted in the figure with a blue box, and segmentations obtained using the combination of parameters resulting in this highest correlation are also displayed in the figure shown below. Parameters yielding highest correlation for Tb.Th attempt to minimize the thickness of trabecular structures within the ROI such that it can replicate the values obtained from Micro-CT. By doing so we see that the segmentation algorithm tends to erode regions of trabecular structures within the ROI. The combination of parameters resulting in highest correlation for Tb.Sp generates segmentations such that the cavities between the trabecular micro-structures are similar to those in Micro-CT. This may potentially bias the estimation of trabecular ridge thickness within the ROI. Similarly if we look at BV/TV, the segmentation resulting the highest correlation does not retrieve all the trabecular structures within the ROI. Figure 12 also shows the behavior of correlation values for the parameter sweep performed on FPD-CBCT and Conventional MDCT. The red

box represents the optimal combination of parameter selected for each system. The optimal combination of parameters was selected based on visual inspection of the segmentations. From the correlation values obtained we can see that CMOS-CBCT performs better than conventional MDCT for all Bernsen algorithm

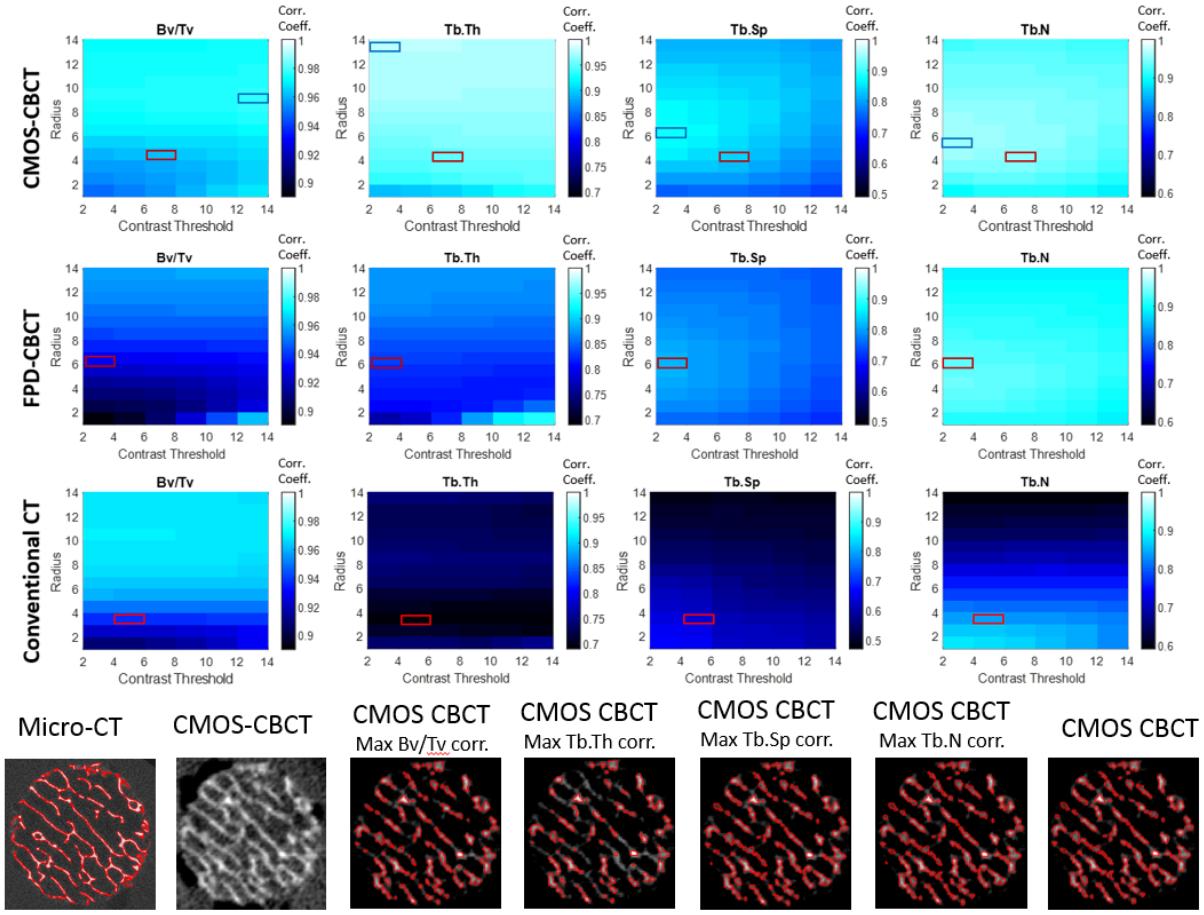

Figure 12: Correlation coefficients computed for bone metrics obtained from segmentations after parameter sweep for Conventional CT (4th Row), FPD-CBCT (3rd Row) and CMOS-CBCT (2nd Row). The red box indicates the correlation coefficient for the selected combination of parameters. The blue box in the 2nd Row indicates the combination of parameters resulting in highest correlation. Micro-CT and CMOS-CBCT segmentations for resulting in highest correlation for each bone metric.

parameters. Overall performance for conventional MDCT is lower than that of CMOS-CBCT.

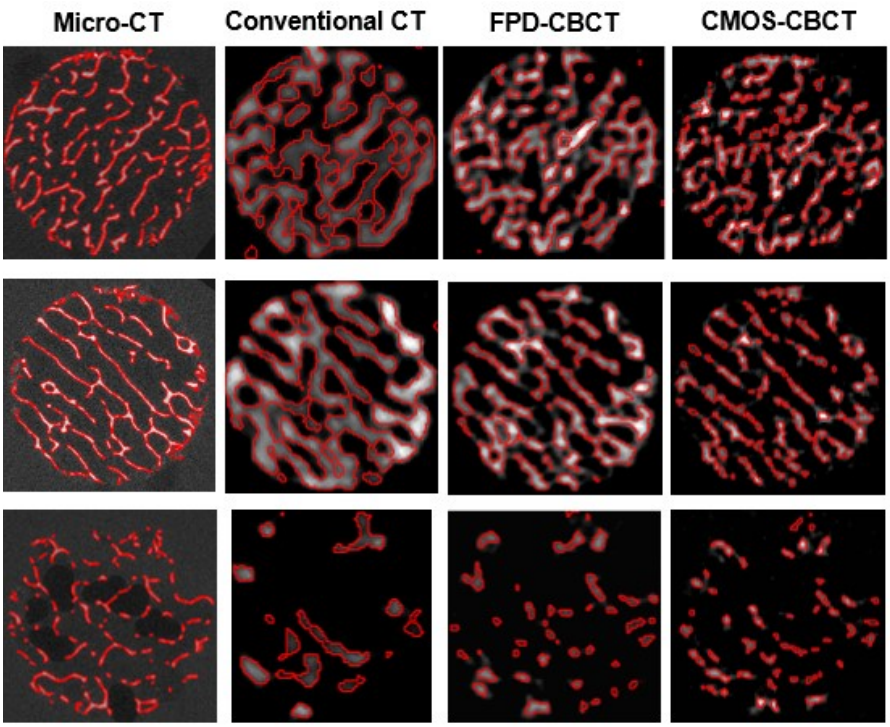

Figure 13 : Axial slices of Micro-CT segmentations (left column) of three example trabecular bones cores compared to Conventional MDCT segmentations (2nd Column), FPD-CBCT(3rd Column) and CMOS-CBCT (4th Column). The segmentations in red are overlayed on the global pre-thresholded grayscale images

The optimal segmentations obtained from the volumes after global pre-thresholding (background) are shown below in figure 13 red (overlay). The 1st column has Micro-CT segmentations of the bone cores. The CMOS-CBCT shows better delineation of trabecular microstructures as compared to FPD-CBCT and Conventional MDCT (2nd and 3rd column). CMOS-CBCT yields thinner structures of trabeculae. The bone metric measurements from CMOS-CBCT, FPD-CBCT and conventional CT are compared to gold standard Micro-CT in Figure 14. In this plot each point represents the mean metric value measured inside the ROI for a single sample. CMOS-CBCT achieved better correlations with Micro-CT for all metrics.

The Pearson correlation coefficient for trabecular thickness (Tb.Th) showed substantial increase in CMOS-CBCT from conventional CT (from 0.7 to 0.96) and FPD-CBCT (0.84 to 0.96), as anticipated based on the reduced blurring seen in the trabeculae of CMOS-CBCT. The spread of values about the trendline reduced with CMOS-CBCT samples.

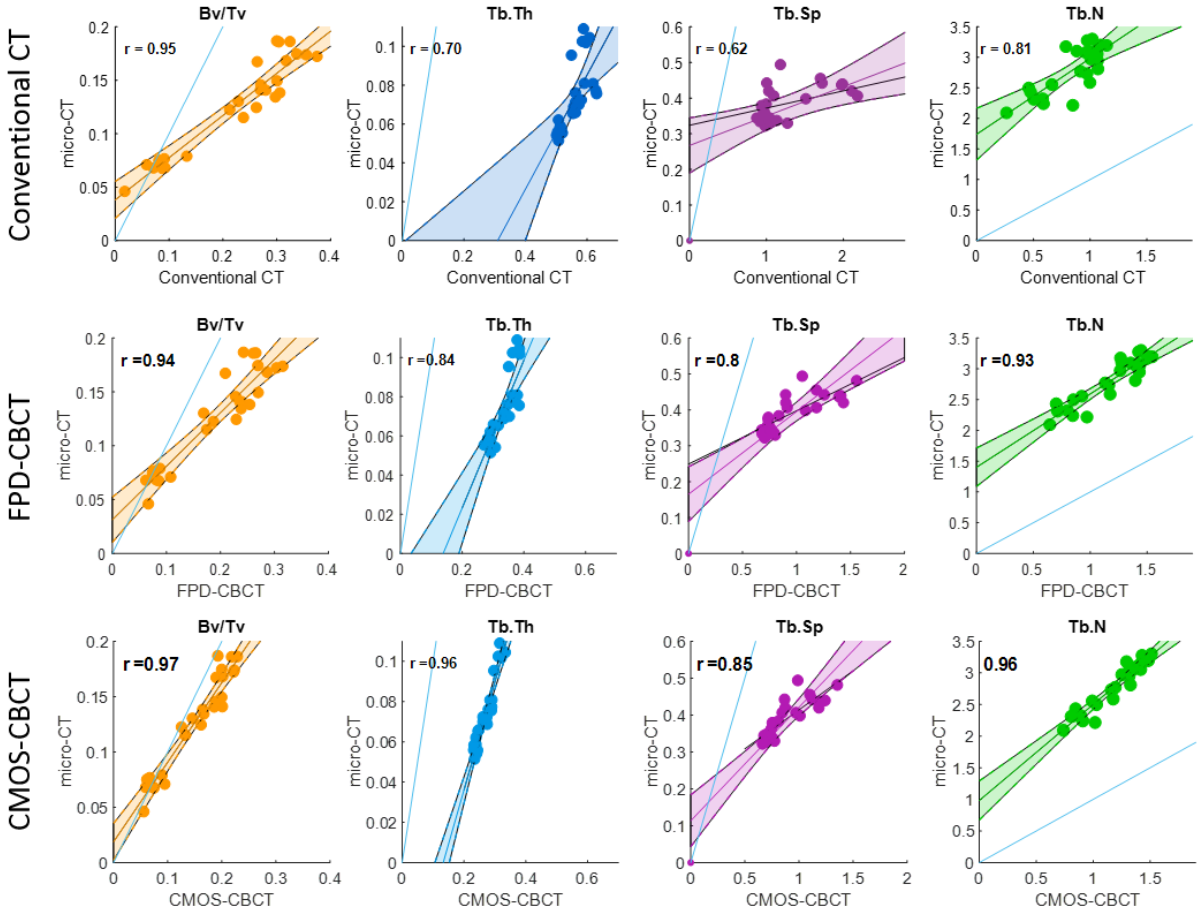

Figure 14: Comparison of metrics of trabecular microarchitecture derived from Convention CT (MDCT – 1st Row), FPD-CBCT (2nd row) and CMOS-CBCT (3rd Row) to reference Micro-CT. Pearson coefficient is reported at top left corner of each graph. The blue dotted line is the Identity line.

3.1.1 Effects of Resolution in Extremity CBCT

To test the effect of spatial resolution on quantitative analysis of bone metrics, measurements were obtained from the segmentations of 35 transiliac bone biopsy samples. Three samples representing the range of BV/TV in the study were selected and are shown in the Figure 15. The first two columns show axial slices from Micro-CT of the samples. The first column shows grayscale images of the axial slices, the second column shows the segmentation in red. The next two columns show grayscale axial slices and segmentations of CBCT data reconstructed with no binning and the last two columns show FPD-CBCT data reconstructed using 2x2 binning.

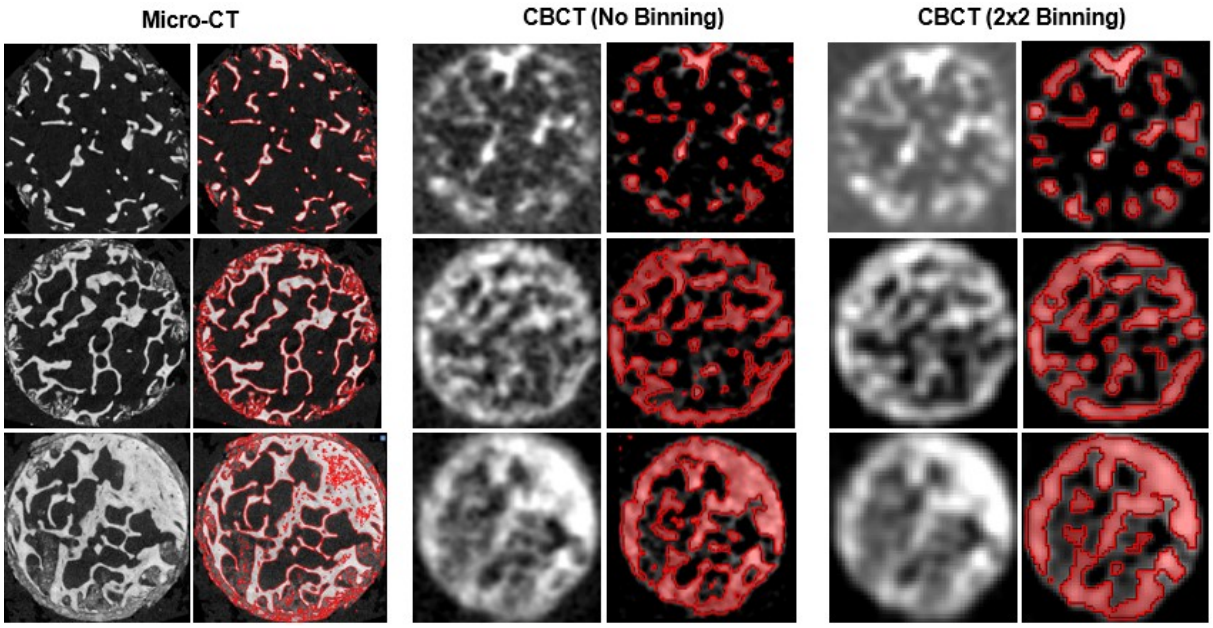

Figure 15: Axial Slices of 3 Micro-CT (1st Column) samples, its segmentation (2nd column), FPD-CBCT reconstructions (no binning, 3rd and 4th column) and FPD-CBCT reconstructions (with 2x2 binning)

The detail in trabecular structure reduces with binning. Grayscale images of the FPD-

CBCT axial slices with no binning have less blurring. However, a fair estimate of the fraction of bone in the ROI can be determined even after binning. Pearson correlation coefficient for BV/TV of CBCT (with 2x2 binning) with reference Micro-CT is 0.92. Figure 16 below shows how FPD-CBCT with binning and without binning perform with reference gold standard Micro-CT.

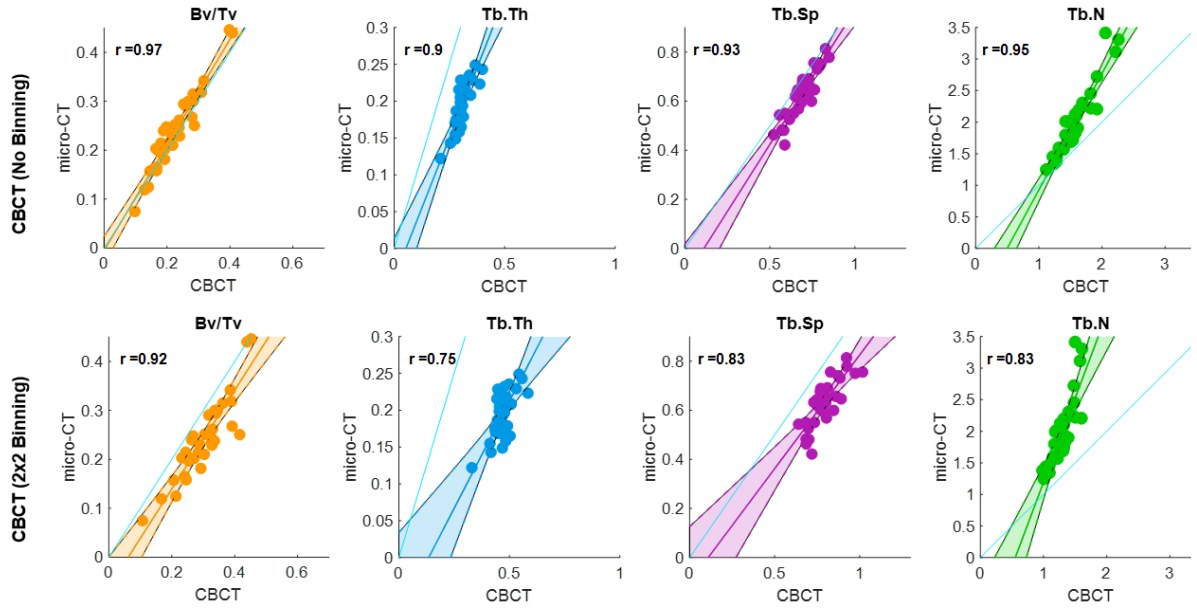

Figure 16: Comparison of metrics of trabecular microarchitecture derived from FPD-CBCT (with no binning - 1st row) and FPD-CBCT (with 2x2 binning – 2nd row) with reference Micro-CT. The Pearson correlation for each metric is in the top left corner.

FPD-CBCT (with no binning) results in better correlations. FPD-CBCT (with 2x2 binning) shows reasonable performance being able to detect regions of trabecular bone and also the spacing between the trabecular structures. BV/TV can be considered independent of the trabecular microarchitecture, since it merely represents the total

number of bone voxels within the ROI. Tb.Th and Tb.Sp convey more information regarding the structure in itself.

3.2 Evaluation of UHR-MDCT

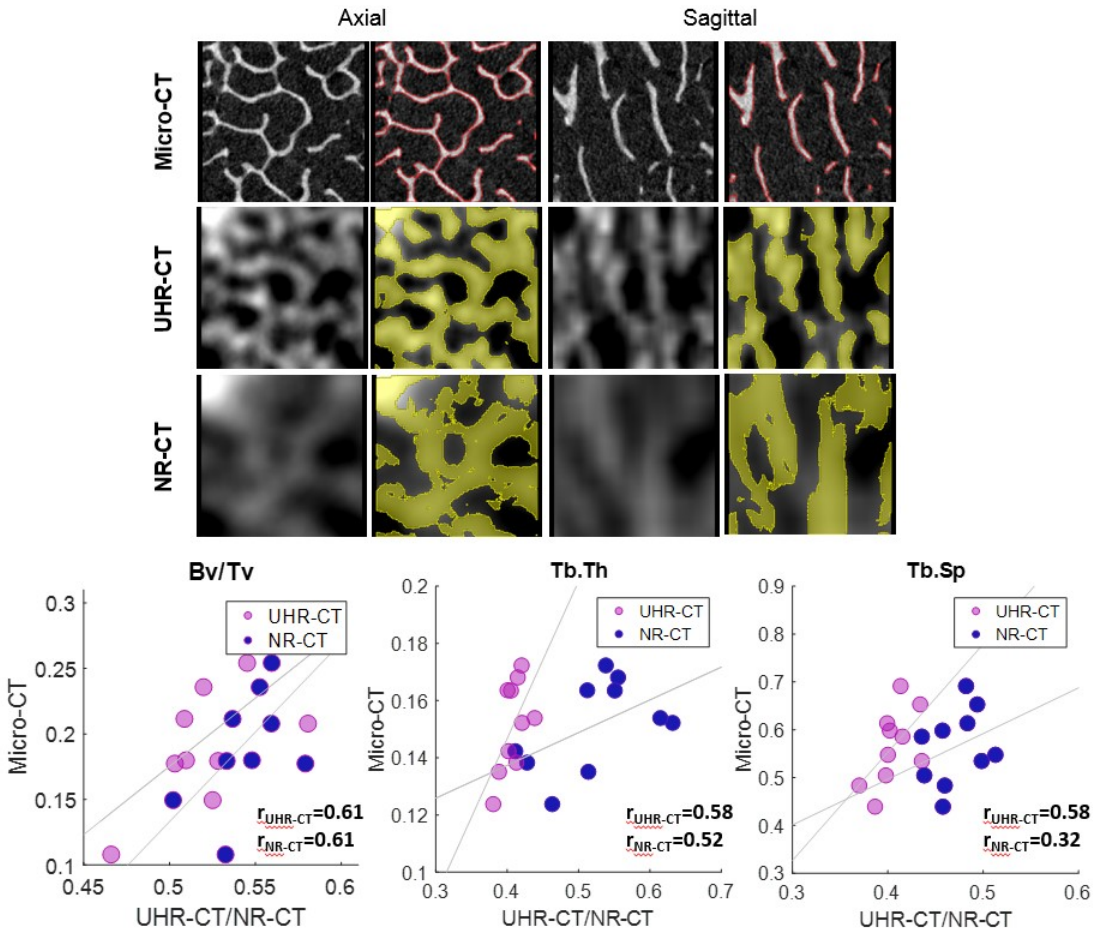

Figure 17: Axial and Sagittal views of an ROI with its segmentations. Bone metrics of trabecular microarchitecture derived from UHR-MDCT and NR-MDCT.

The UHR-MDCT system in UHR mode improves quantitative assessment of vertebral microarchitecture compared to standard MDCT, enabling more accurate estimation of fracture risk. The study involved analysis of small regions within the ulna to compute bone metrics and determine the performance of the UHR-MDCT system in comparison to normal resolution NR-MDCT. The UHR-MDCT images show good

delineation of trabecular structures. Figure 17 shows the detail in trabecular structure and the segmentations obtained after applying Bernsen's algorithm to the ROI's. The parameters for the thresholding algorithm were selected so that the correlations for BV/TV (fairly insensitive to spatial resolution) against Micro-CT were comparable for both UHR-MDCT and NR-MDCT, with the Pearson correlation coefficient for BV/TV of ~0.61. For Tb.Th UHR-MDCT showed a correlation of 0.58 whereas, NR-CT showed 0.52. There was a ~80% improved correlation for Tb.Sp, 0.58 for UHT-CT vs. 0.32 for NR-CT.

3.3 RT Patient Data Processing

This study involved collecting and processing patient data to test the feasibility of the extremity FPD-CBCT system in evaluating trabecular structures *in-vivo*.

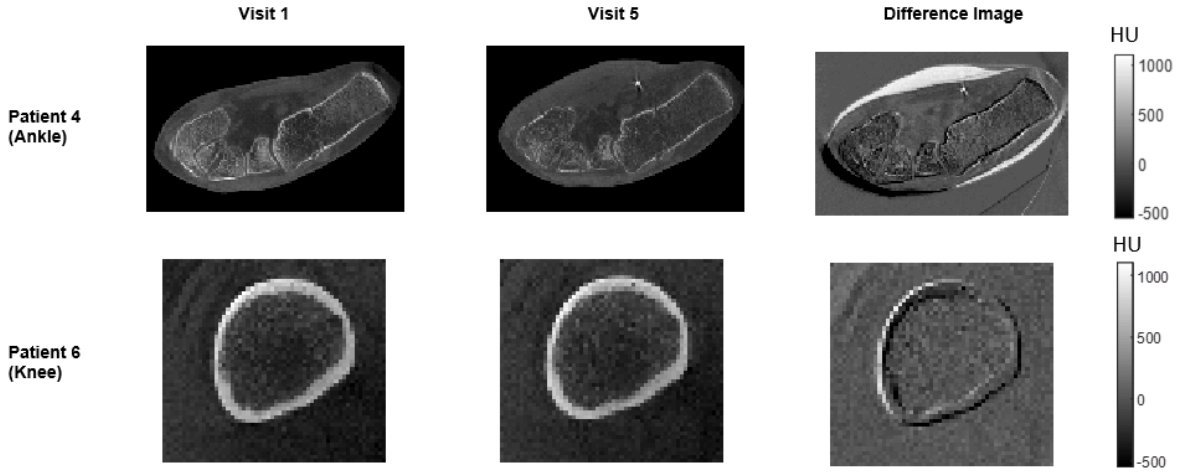

Figure 17: Axial slices of image reconstruction of visit 1 for patient 4 and 6 (1st column), visit 5 (2nd column) and difference image (3rd column)

The available dataset has a range of patient data. The data was reconstructed for the first and last visits for the affected and unaffected extremity, following which the two-

step registration was performed. Figure 18 shows an axial slice of the reconstructed image volumes. The 1st column corresponds to the 1st visit, the 2nd column is the registered view of the final visit made and the last column shows the axial slice of a difference image generated from the two image volumes. Only slight residual registration is observed in the difference images.

To improve the quality of the images, scatter correction using Monte-Carlo (MC) simulations was done [17]. This helped improve the contrast of the bone. Initial evaluation of the MC scatter correction was performed on water calibration phantoms that were scanned during patient visits to monitor CT number uniformity of the system. Figure 19 shows the axial slice of a water phantom reconstructed with and without MC correction.

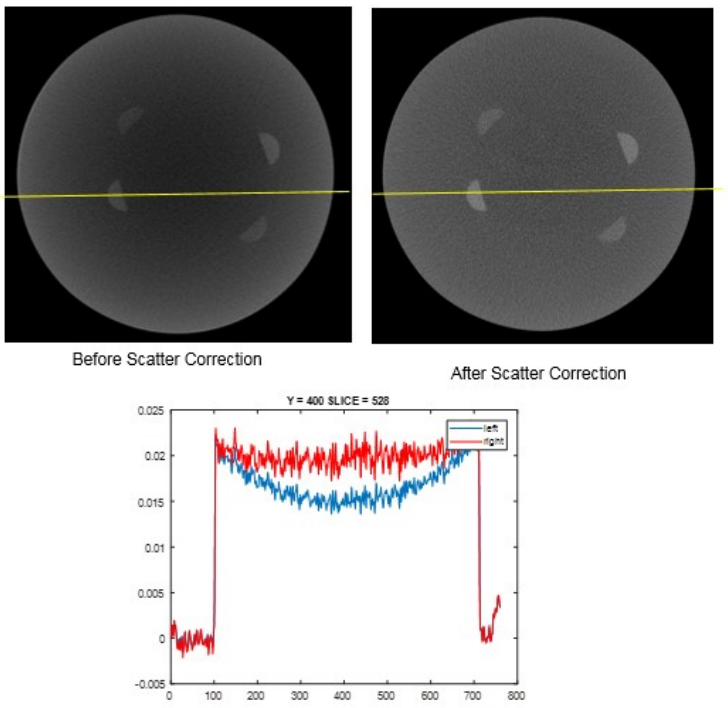

Figure 19: Axial slice of water phantom before and after scatter correction along with a line profile of the phantom in the center.

The left slice shows the image before applying scatter correction. The right image is after applying scatter correction. Analyzing the line profile of the sample, we can see that scatter correction has reduced cupping effect visibly. The water phantoms consist of BMD calibration

rods each 0 mg/mL, 75 mg/mL CaHA and 150 mg/mL CaHA. The voxel attenuation values for each of these calibration rods was analyzed before and after scatter correction, and the spread of these values across multiple time points was assessed. The scans for these water phantoms were collected during each patient visit. The data represented here show how the values of attenuation coefficient of the inserts in the volume behave across all available water phantom scans. Figure 20 shows the distribution of the attenuation coefficients of the inserts in the water phantom before and after scatter correction. We can see that the spread in values decreases, and the values inside the water phantom are more uniform post scatter correction.

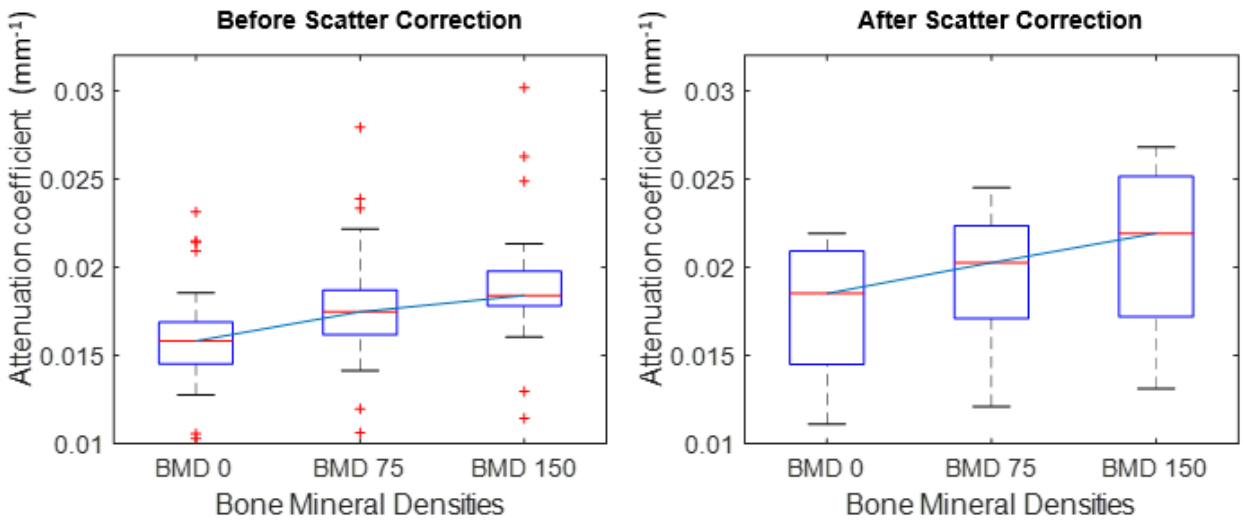

Figure 20: Distribution of grayscale values of the calibration rods inside the water phantom before and after scatter correction.

The attenuation coefficient for water is close to 0.02 mm^{-1}. We can see that before scatter correction the mean value for water, i.e. the BMD insert 0 is ~0.0158 mm^{-1} and after scatter correction the mean value is ~0.019 mm^{-1}, which is closer to the attenuation

coefficient of water. The spread of values also decreases due to improved image uniformity. The difference between the minimum and maximum value in the dataset before scatter correction for BMD insert 0 mg/mL (water) is 0.013, for BMD insert 75 mg/mL is 0.0173 and for BMD insert 150 mg/mL is 0.0193. The difference in values after scatter correction for BMD insert 0 mg/mL is 0.11, for BMD insert 75 mg/mL is 0.013 and for BMD insert 150 mg/mL is 0.014. From the plots above we can also see that the attenuation coefficients were more linear after scatter correction.

Scatter correction was next applied to the patient data. Figure 21 shows the effect of scatter correction on an example axial slice of the scan of a knee. There is a visible improvement in the contrast of the bone in the image after scatter correction. The image before correction also shows cupping effect within the bone region due to scatter. A table with details of data available for each patient visit and the updates on the stages of data processing implemented for each patient using the above discussed pipeline has been added to the appendix of this thesis. The appendix also has processed images of the axial slices of the first and last visit for each patient. It summarizes the ongoing analysis of data. The images also illustrate the complexities of registration across a longitudinal series of scans, which is challenged by soft-tissue

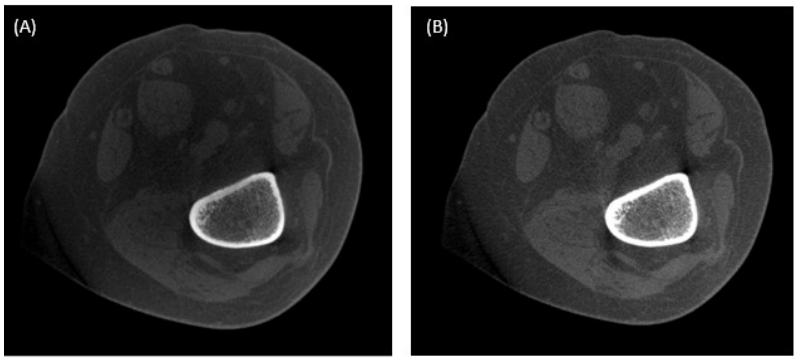

Figure 21: (A) Axial slice of knee before scatter correction and (B) after scatter correction

deformation and independent displacements of individual bones. Despite the inherent limitations of rigid registration in this context, it is applied here to provide a starting point for manual ROI selection for bone analysis using methods in Sec 3.1 - 3.2.

CHAPTER 4

Conclusion

CBCT shows favorable performance in spatial resolution and quantitative imaging of trabecular microarchitecture in comparison to conventional MDCT. It achieves better correlation with Micro-CT, especially for bone metrics such as Tb.Th and Tb.Sp. Among the CBCT systems, CMOS-based CBCT provided improved performance in quantification of bone microstructure while retaining weight-bearing capabilities of FPD-CBCT. This result is due to the high spatial resolution achieved by CMOS-CBCT by means of smaller detector pixel size of (99 μm) and reduced scintillator thickness. CMOS-CBCT has ~4x shorter scan time and ~40% increase in spatial resolution (FWHM od a ~0.1 mm tungsten wire [7]). The reduced scan time helps reduce the artifacts introduced due to motion. It was observed that CMOS-CBCT improves correlation with Micro-CT compared to FPD-CBCT. Measurements of trabecular spacing (Tb.Sp) benefited the most from enhanced spatial resolution. Tb.Sp correlation with Micro-CT was seen to be 0.7 for MDCT, 0.84 for FPD-CBCT and 0.96 for CMOS-CBCT.

Similarly to extremity CBCT, UHR-MDCT images obtained using the Precision CT system also showed improved quantification of bone microarchitecture in

comparison to standard resolution MDCT. Tb.Th correlation with Micro-CT was 0.52 for NR-MDCT and 0.58 for UHR-MDCT. Tb.Sp correlation with Micro-CT was 0.32 for NR-MDCT and 0.58 for UHR-MDCT. The structural information obtained using UHR-MDCT will enable BMD measurement in the spine and hips to assess risk of fractures in individuals with osteoporosis. BV/TV as a bone metric can be said to be relatively independent of the spatial resolution as it represents the total number of bone voxels within a ROI. On the other hand, Tb.Th and Tb.Sp are highly dependent on the resolution of the imaging modality and its capability to represent actual thickness and spacing between trabecular ridges.

Patient data obtained from the extremity CBCT scanner can be seen to show better bone contrast after scatter correction. The processing pipeline developed in this work, including image registration and artifact correction, will be essential to future longitudinal studies of bone health in human subjects following RT.

Overall, the recently developed high resolution CT technologies are promising for evaluation of i*n-vivo* trabecular microarchitecture. Their introduction into clinical practice may enable development of new quantitative biomarkers of bone health to augment conventional measurements of BMD. UHR-MDCT is a similarly innovative technology that achieves higher resolution than conventional MDCT systems and also supports more accurate analysis of quantitative metrics of bone morphology.

References

1. Hootman JM, Helmick CG, Barbour KE, Theis KA, Boring MA. Updated projected prevalence of self-reported doctor-diagnosed arthritis and arthritis-attributable activity limitation among US adults, 2015–2040. *Arthritis & Rheumatol.* 2016;68(7):1582–1587. doi: 10.1002/art.39692. PubMed PMID: 27015600.
2. Brehler, M., Cao, Q., Moseley, K.F., Osgood, G., Morris, C., Demehri, S., Yorkston, J., Siewerdsen, J.H. & Zbijewski, W. 2018, "Robust quantitative assessment of trabecular microarchitecture in extremity cone-beam CT using optimized segmentation algorithms", Progress in Biomedical Optics and Imaging - Proceedings of SPIE.
3. Weinans, H., Siebelt, M., Agricola, R., Botter, S.M., Piscaer, T.M., Waarsing, J.H., "Pathophysiology of peri-articular bone changes in osteoarthritis" Bone, 51, 190–196 (2012).
4. Bernsen, J (1986), "Dynamic Thresholding of Grey-Level Images", *Proc. of the 8th Int. Conf. on Pattern Recognition*
5. Nobuyuki Otsu (1979). "A threshold selection method from gray-level histograms". *IEEE Trans. Sys., Man., Cyber.* **9** (1): 62–66. doi:10.1109/TSMC.1979.4310076
6. Cao Q, Brehler M, Sisniega A, et al. High-resolution extremity conebeam CT with a CMOS detector: task-based optimization of scintillator thickness. Proc. SPIE. 2017; 10132:1–6.
7. J. A. Carrino, A. Al Muhit, W. Zbijewski, G. K. Thawait, J. W. Stayman, N. Packard, R. Senn, D. Yang, D. H. Foos, J. Yorkston, and J. H. Siewerdsen, "Dedicated cone-beam CT system for extremity imaging.," *Radiology*, vol. 270, no. 3, pp. 816–24, Mar. 2014.
8. Q. Cao, M. Brehler, A. Sisniega, S. Tilley, M. M. Shiraz Bhurwani, J. W. Stayman, J. Yorkston, J. H. Siewerdsen, and W. Zbijewski "High-resolution extremity cone-beam CT with a CMOS detector: evaluation of a clinical prototype in quantitative assessment of bone microarchitecture", Proc. SPIE 10573, Medical Imaging 2018: Physics of Medical Imaging, 105730R (9 March 2018); doi: 10.1117/12.2293810; https://doi.org/10.1117/12.2293810

9. Li, G., Yin, J., Gao, J., Cheng, T. S., Pavlos, N. J., Zhang, C., & Zheng, M. H. (2013). Subchondral bone in osteoarthritis: insight into risk factors and microstructural changes. Arthritis research & therapy, 15(6), 223. doi:10.1186/ar4405

10. Link T, Bauer J. Imaging of Trabecular Bone Structure. Seminars in Musculoskeletal Radiology 2002; 06(03): 253 - 262. doi:10.1055/s-2002-36723
11. Hildebrand, T. and Rüegsegger, P., "A new method for the model-independent assessment of thickness in three-dimensional images." J Microscopy, 185(1):67-75 (1997).
12. Looker A, Melton III L, Borrud L, Shepherd J. Lumbar spine bone mineral density in US adults: Demographic patterns and relationship with femur neck skeletal status. *Osteoporos Int*. 2012;23(4):1351-1360. Doi: 10.1007/s00198-011-1693-z.
13. Cooper C, Atkinson EJ, O'Fallon WM, Melton LJ., 3rd Incidence of clinically diagnosed vertebral fractures: a population-based study in Rochester, Minnesota, 1985–1989. J Bone Miner Res. 1992;7:221–7
14. Osterhoff G, Morgan EF, Shefelbine SJ, Karim L, McNamara LM, Augat P. Bone mechanical properties and changes with osteoporosis. *Injury*. 2016;47 Suppl 2(Suppl 2):S11–S20. doi:10.1016/S0020-1383(16)47003-8
15. Waarsing JH, Day JS, Weinans H. An improved segmentation method for in vivo μCT imaging. *J Bone Miner Res*. 2004;19(10):1640-1650. https://doi.org/10.1359/JBMR.040705. doi: 10.1359/JBMR.040705.
16. Saparin P, Thomsen JS, Kurths J, Beller G, Gowin W. Segmentation of bone CT images and assessment of bone structure using measures of complexity. *Med Phys*. 2006;33(10):3857-3873. https://doi.org/10.1118/1.2336501. doi: 10.1118/1.2336501.
17. A. Sisniega, M. Abella, E. Lage, M. Desco, J. J. Vaquero. Automatic monte-carlo based scatter correction for X-ray cone-beam CT using general purpose graphic processing units (GP-GPU): A feasibility study. *2011 IEEE Nuclear Science Symposium Conference Record*. 2011:3705-3709. doi: 10.1109/NSSMIC.2011.6153699.
18. Sisniega, A., Stayman, J. W., Yorkston, J., Siewerdsen, J. H., & Zbijewski, W. (2017). Motion compensation in extremity cone-beam CT using a penalized image sharpness criterion. *Physics in Medicine & Biology*, *62*(9), 3712.

19. S. Subramanian, M. Brehler, Q. Cao, F. J. Quevedo Gonzalez, R. E. Breighner, J. A. Carrino, T. Wright, J. Yorkston, J. H. Siewerdsen, W. Zbijewski, "Quantitative evaluation of bone microstructure using high-resolution extremity cone-beam CT with a CMOS detector," Proc. SPIE 10953, Medical Imaging 2019: Biomedical Applications in Molecular, Structural, and Functional Imaging, 1095317 (15 March 2019);
20. Willey JS, Lloyd SA, Nelson GA, Bateman TA. Ionizing Radiation and Bone Loss: Space Exploration and Clinical Therapy Applications. *Clin Rev Bone Miner Metab.* 2011;9(1):54–62. doi:10.1007/s12018-011-9092-8
21. A. Syed and T.A. Damron, "Post-radiation fractures in the setting of lower extremity soft-tissue sarcoma treatment," J. Radiat. Oncol. 3(2), 205–213 (2014).
22. Mazess, R.B. Calcif Tissue Int (1987) 41: 117. https://doi.org/10.1007/BF02563789

APPENDIX

Patient Number	Extremity Scanned	Number of visits	Number of visits Reconstructed	One year follow up scan available	Registration Performed:	Scatter Correction performed
1	Knee (Left Affected)	5	2 (visit 1 and visit 5)	Yes (visit 5)	Yes (visit 1 and visit 5)	Yes (visit 1 and visit 5)
2	Knee (Right Affected)	5	2 (visit 1 and visit 5)	Yes (visit 5)	Yes (visit 1 and visit 5)	Yes (visit 1)
3	Ankle (Right Affected)	4	2 (visit 1 and visit 4)	Yes (visit 4)	No	No
4	Ankle (Right Affected)	5	2 (visit 1 and visit 5)	Yes (visit 5)	Yes (visit 1 and visit 5)	Yes (visit 1)
6	Knee (Right Affected)	5	2 (visit 1 and visit 5)	Yes (visit 5)	Yes (visit 1 and visit 5)	Yes (visit 1)
7	Knee (Right Affected)	5	2 (visit 1 and visit 5)	Yes (visit 5)	Yes (visit 1 and visit 5)	No
8	Ankle (Right Affected)	4	2 (visit 1 and visit 4)	No	Yes	No
9	Ankle (Right Affected)	3	2 (visit 1 and visit 3)	No	Yes	No
10	Knee (Left Affected)	5	2 (visit 1 and visit 4)	No	Yes	No
11	Knee (Left Affected)	4	2 (visit 1 and visit 4)	No	Yes	No
12	Hand (Left Affected)	4	2 (visit 1 and visit 4)	No	Yes	No

13	Knee (Right Affected)	1	1 (visit 1)	No	No	No
14	Hand (Right Affected)	1	1 (visit 1)	No	No	No
15	Knee	3	None	No	No	No
16	Knee	3	None	No	No	No
17	Knee	3	None	No	No	No

Table 2: Log of patient data available and update of data processing performed on each dataset

Example images from preliminary analysis of patient data are shown below. All scans were adjusted between 300 HU and 1500 for display purposes.

Patient 1: Figure showing registered axial slice of 1st and 5th visit of the affected left knee. The images shown here involved an initial, preliminary application of scatter correction. Further optimization of the correction pipeline is ongoing. The registration was performed using an ROI placed on the femur, hence we can see substantial amount of deformation with regard to soft tissue. All images were adjusted between 300-1500 HU for display purposes.

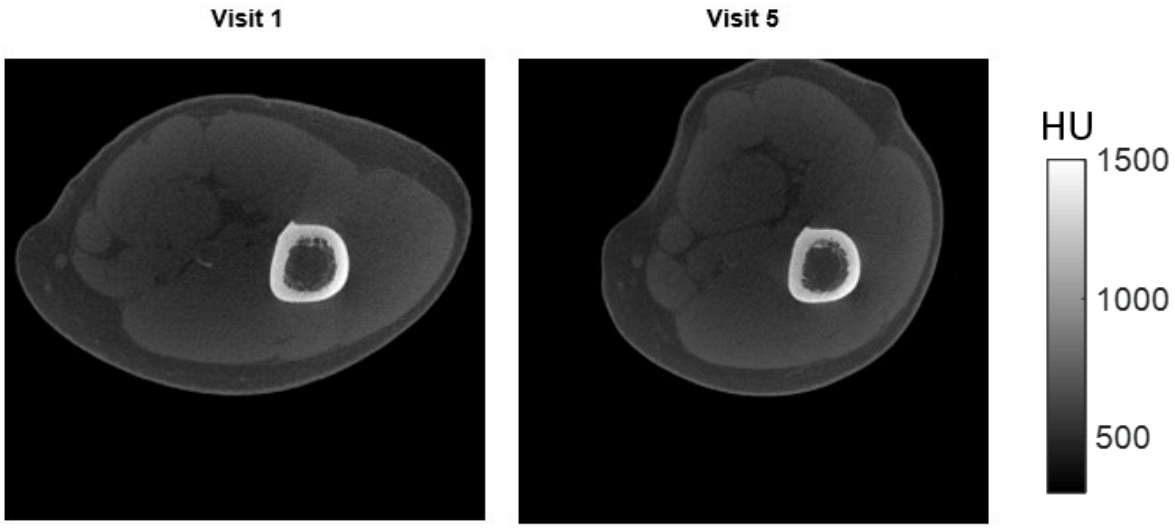

Patient 2: Figure showing registered axial slice of 1st and 5th visit of the right affected knee. The images shown here involve an initial, preliminary application of scatter correction. The registration was performed using an ROI placed on the lower end of the femur. Further optimization of the correction pipeline is ongoing.

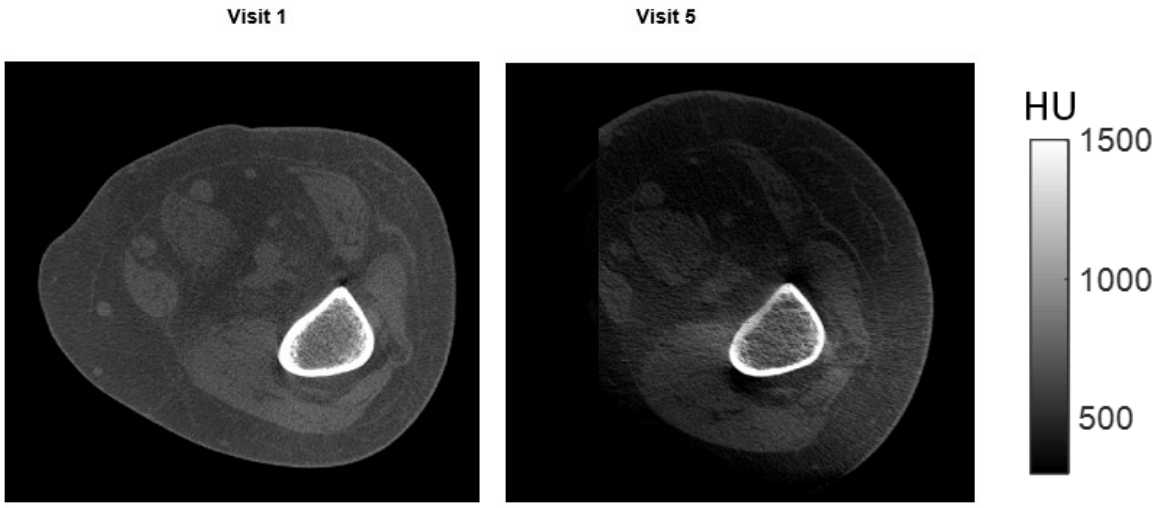

Patient 4: Figure showing registered sagittal slice of 1st and 5th visit of the right affected ankle. Registration was performed using an ROI on the calcaneus and a part of the talus. Further optimization of the correction pipeline is ongoing.

Patient 6: Figure showing registered axial slice of 1st and 5th visit of the right affected knee. The registration was performed using an ROI placed on the femur. These scans are not scatter corrected.

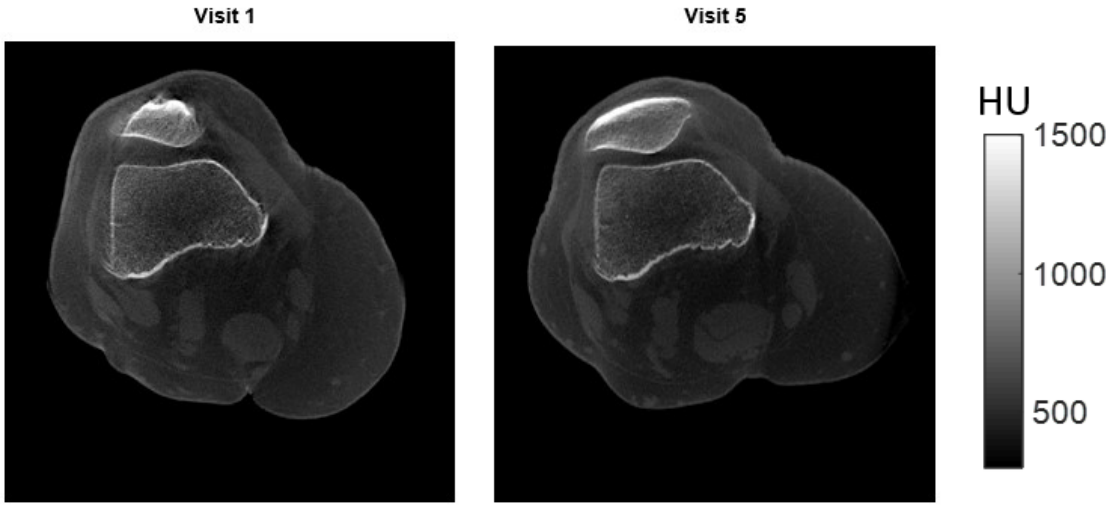

Patient 7: Figure showing registered axial slice of 1st and 5th visit of the right affected knee. The registration was performed using an ROI placed on the lower end of the femur. These scans are not scatter corrected.

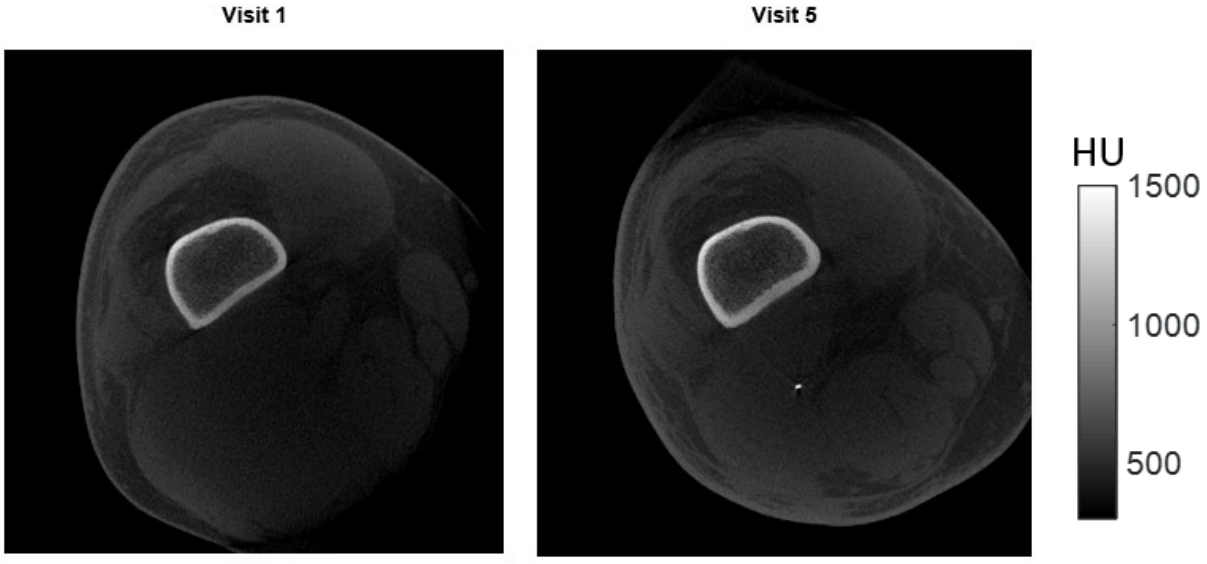

Patient 8: Figure showing registered sagittal slice of 1st and 4th visit of the right affected ankle. Registration was performed using an ROI on the talus and a part of the tibia. These scans are not scatter corrected.

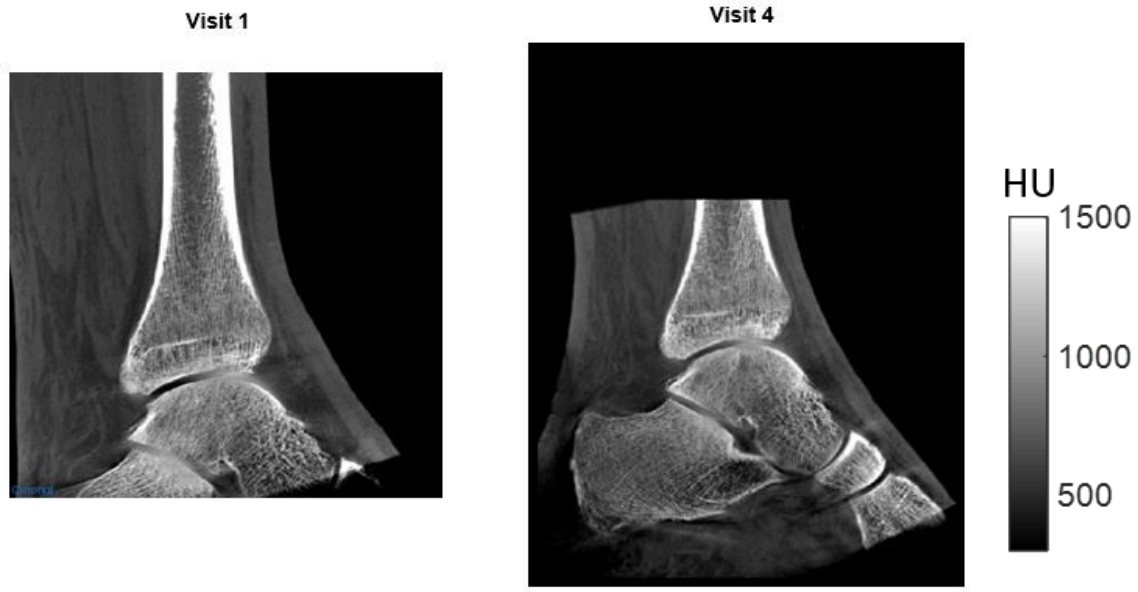

Patient 9: Figure showing registered sagittal slice of 1st and 3rd visit of the right affected ankle. Registration was performed using an ROI on the calcaneus. These scans are not scatter corrected.

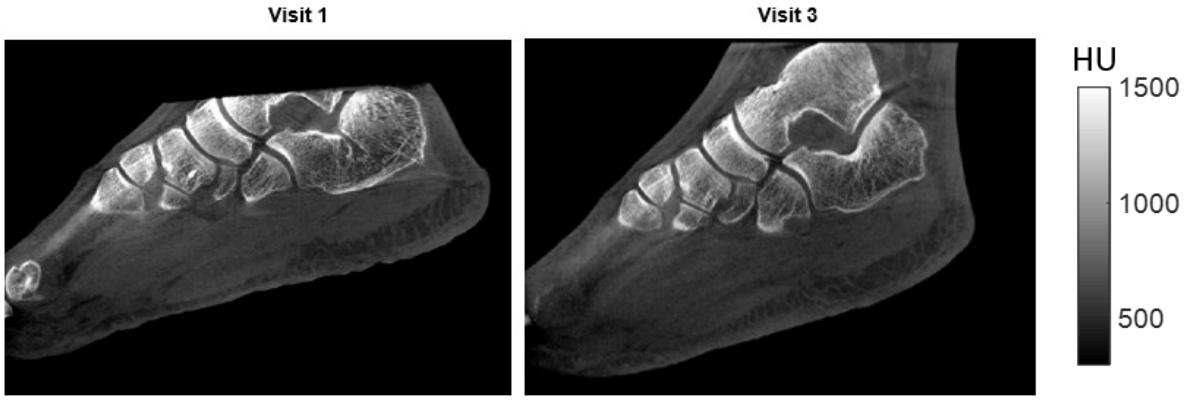

Patient 10: Figure showing registered axial slice of 1st and 4th visit of the left affected knee. Registration was performed using an ROI on the femur. These scans are not scatter corrected.

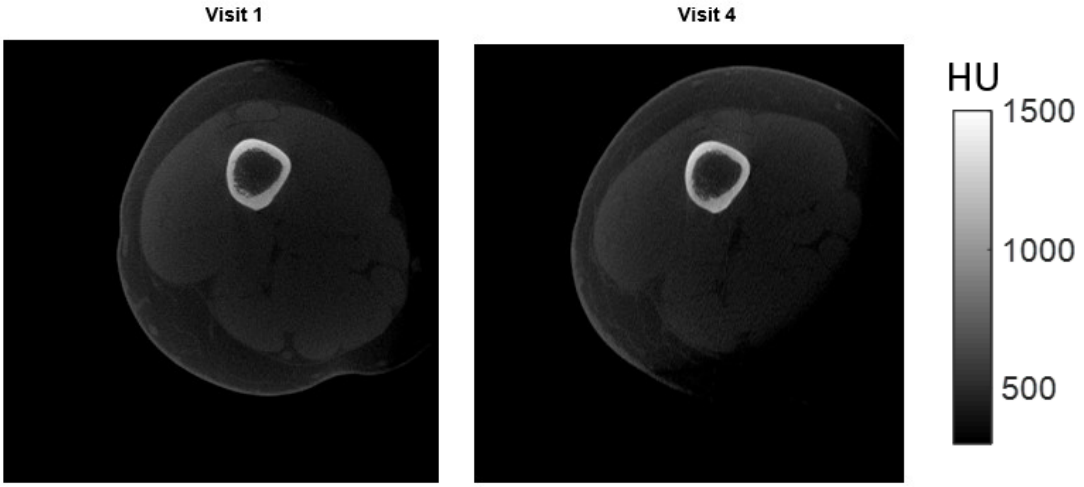

Patient 11: Figure showing registered axial slice of 1st and 4th visit of the left affected knee. Registration was performed using an ROI on the femur. These scans are not scatter corrected.

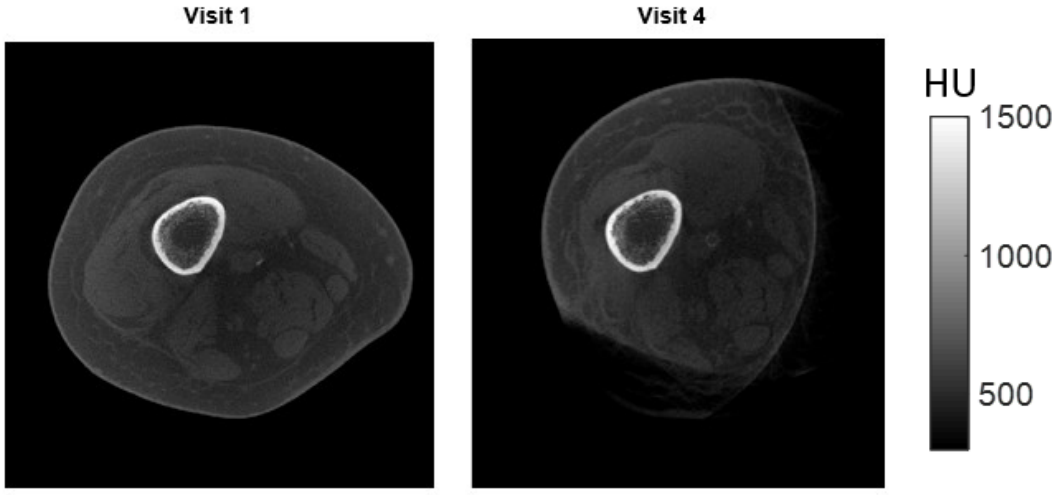

Biography

Shalini Subramanian was born in 1995 in India.

She did her undergraduate work at Dwarkadas J. Sanghvi College of Engineering, University of Mumbai where she majored in Biomedical Engineering. In 2017, she began her M.S.E Biomedical engineering at Johns Hopkins University.